Photon Efficiency Measurements using Radiative Z Decays with the ATLAS Detector

Fionn Bishop, University of Cambridge

September 6, 2018

Abstract

Modifications to the method of measuring photon efficiencies in radiative Z decays are proposed and the results of their implementation are presented. These efficiencies are calculated in bins of photon transverse momentum p_T^γ and pseudorapidity $|\eta^\gamma|$, and separately for converted and unconverted photons, and electrons and muons. The backgrounds $Z \to \tau\tau j$, $t\bar{t}\gamma$ and WZ are considered in addition to the dominant background $Z \to \ell\ell j$. The inclusion of $Z \to \tau\tau j$ may significantly affect the efficiency measurement, whereas $t\bar{t}\gamma$ and WZ are insignificant. A missing irreducible background is located at $p_T^\gamma < 20$ GeV and three-body invariant mass $m_{\ell\ell\gamma} < 80$ GeV. It is suggested that this is $Z \to \tau\tau\gamma$, and that the exclusion of this background may result in a significant error on the efficiency. The reducible background template from Monte Carlo is replaced with a template from data in an anti-isolation, anti-ID control region, with $|\eta^\gamma|$ bins grouped, which is fitted to a double sided crystal ball function. This improves the statistical power of the template in most regions, particularly $20 < p_T^\gamma < 40$ GeV, but statistics are very poor in the region $p_T^\gamma > 40$ GeV, $m_{\ell\ell\gamma} < 80$ GeV. The use of only unprescaled triggers, and associated p_T^ℓ cuts to mitigate the effects of turn-on, are included in event selection cuts to significantly improve data-Monte Carlo agreement. This modified method led to the successful evaluation of the ID efficiency (number of events passing ID and isolation cuts/number of events passing isolation cuts) and the total efficiency (number of events passing ID and isolation cuts/total number of events).

1 Introduction

Photons are present in many important physics processes which are studied in the ATLAS detector, including $H \to \gamma\gamma$ [3] and BSM processes such as the decay of supersymmetric particles [5, 4]. In studying these processes, photon isolation and identification (ID) selection criteria applied to data samples are necessary to exclude the reducible backgrounds that arise as a result of photons from hadronic decays or the reconstruction of jets or leptons as photons. These selection criteria (cuts) are very effective at reducing background, but also exclude some signal events. To accurately study the processes described above, it is necessary to know the fraction of signal photons that are excluded by these cuts. This is the efficiency:

$$\epsilon = \frac{N_S[\text{cut}]}{N_S} \tag{1}$$

It is possible to estimate this quantity using Monte Carlo (MC) simulation, but this leads to large uncertainties as a result of an imperfect description of showering in the detector [1] and ultimately, it is important to have a measurement from data. Three methods of obtaining a

data-driven measurement of ϵ exist [6, 1], which are each useful in a different photon transverse momentum (p_T^γ) range. The method considered in this report measures photon efficiencies in the radiative Z decay $Z \to \ell\ell\gamma$. A Z boson formed in a Drell-Yan process decays to two same-flavour leptons, and a photon is emitted either as ISR (by one of the initial state quarks; figure 1) or FSR (by one of the final state leptons; figure 2). This process is used because it is well-understood and has a reasonably high cross section. It is useful in the range $10 < p_T^\gamma < 100$ GeV, because photons with $p_T^\gamma < 10$ GeV cannot be accurately reconstructed in the detector, and the the cross section for $Z \to \ell\ell\gamma$ events with $p_T^\gamma > 100$ GeV is too small to produce a sufficient number of events to analyse.

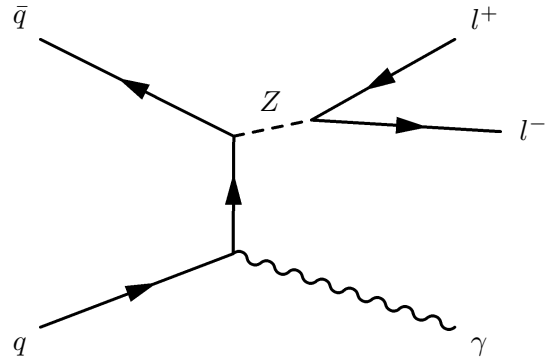

Figure 1: The radiative Z decay with an ISR photon. A photon is annihilated by an initial state quark. Then two same-flavour quarks annihilate in a Drell-Yan process to form a Z boson, which decays to two same-flavour leptons.

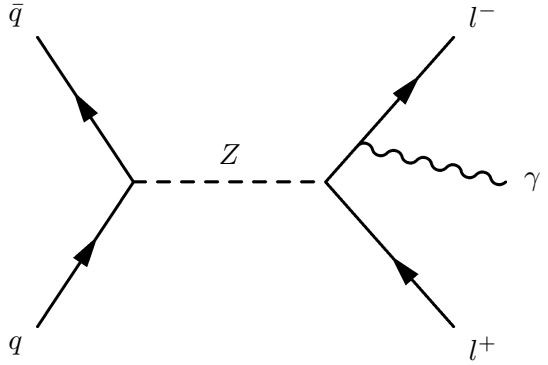

Figure 2: The radiative Z decay with an FSR photon. Two same-flavour quarks annihilate in a Drell-Yan process to form a Z boson, which decays to two same-flavour leptons. Then one final state lepton radiates a photon.

This measurement has been made before [6, 1, 9], but with fractional uncertainties of up to 10%, so there is the potential for improvement. This report discusses several ways in which modifications to the measurement have been implemented with a view to improving precision. The two main modifications are the inclusion of additional backgrounds ($\tau\tau j$, WZ and $t\bar{t}\gamma$), and the use of data from an anti-isolation, anti-ID control region as a background template to reduce background statistical uncertainty. Additionally, the total efficiency (ϵ_{TOT}), which is the number of signal events passing both ID and isolation cuts divided by the total number of signal events, is calculated, in addition to the ID efficiency ϵ_{ID}, as an alternative to the combination of the correlated isolation and ID efficiencies.

Sections 2 and 3 describe the data and Monte Carlo samples used in this analysis and the selection cuts made. Section 4 defines the cuts related to isolation and ID which are made. The relative importance of the different sources of background are discussed in section 5. Section 6 explains the current method and the modifications implemented. Section 7 discusses sources of uncertainty. Section 8 presents efficiency measurements and section 9 suggests further improvements to the method.

2 Data and Monte Carlo samples

2.1 Data samples

The 2017 data set was used in this study. This was collected at $\sqrt{s} = 13$ TeV and has an integrated luminosity of 43.6 fb^{-1}.

2.2 Monte Carlo samples

Version 00-02-03 ntuples[1] of the Monte Carlo samples described in table 1 were used. All slices of each process were included. Cuts were made to samples of the processes $Z \to \ell\ell\gamma$ and $Z \to \ell\ell j$ to avoid overlap: In $Z \to \ell\ell\gamma$, only events with isolated or non-isolated photons were used and in $Z \to \ell\ell j$, FSR photons were excluded.

Process	Name	DSID	Cuts
$Z \to ee\gamma$	Sherpa CT10 $Z \to ee\gamma$	301535-6	ph.truth_type == 14 (IsoPhoton) or 15 (NonIsoPhoton)
$Z \to \mu\mu\gamma$	Sherpa CT10 $Z \to \mu\mu\gamma$	301899-904	
$Z \to eej$	Sherpa 2.2.1 $Z \to eej$ (Z+jet)(MAXHPTV)	364100-27	ph.truth_origin != 40 (FSR photon
$Z \to \mu\mu j$	Sherpa 2.2.1 $Z \to \mu\mu j$ (Z+jet)(MAXHPTV)		
$Z \to \tau\tau j$	Sherpa 2.2.1 $Z \to \tau\tau j$ (Z+jet)(MAXHPTV)	364128-41	
WZ	PowhegPy8EG CT10 $WZ \to \ell\nu\ell\ell$	361601	
$t\bar{t}\gamma$	MadgraphPythia8 $t\bar{t}\gamma$ nonallhad	410389	

Table 1: MC samples used in the analysis

3 Event selection

The following selection criteria were applied to all MC and data samples. The $Z \to \ell\ell\gamma$ selection criteria are identical to those applied in previous measurements [1, 9, 6]. The trigger-based selection criteria are an addition and their importance will be discussed.

3.1 $Z \to \ell\ell\gamma$ selection

All events used in this analysis satisfy:

- Contain at least one primary vertex with at least three associated tracks; and two same-flavour, opposite-sign leptons and one photon
- $40 < m_{\ell\ell} < 83$ GeV
- Electrons: $\Delta R_{min} > 0.2$
- Muons: $\Delta R_{min} > 0.4$

where $\Delta R_{min} = \min\left[\sqrt{(\eta^\ell - \eta^\gamma)^2 + (\phi^\ell - \phi^\gamma)^2}\right]$. The $m_{\ell\ell}$ cut excludes the majority of the ISR background $Z \to \ell\ell j$. The ΔR_{min} cuts reduce the effect on photon isolation of lepton energy deposition inside the photon isolation cone.

3.2 Triggers

Tables 2 and 3 list the unprescaled triggers saved in the version 00-02-03 ntuples, and tables 4 and 5 list the prescaled triggers. Only events that pass at least one of these unprescaled triggers are used. Turn-on is an effect where some leptons below the trigger threshold are included and some leptons above the trigger threshold are excluded. This effect is a result of mis-measurement at the trigger level and is poorly modelled in MC. Therefore p_T^ℓ cuts are made at values slightly above the trigger threshold to avoid this effect and improve data-MC agreement.

[1]Produced using analysis code described in https://twiki.cern.ch/twiki/bin/viewauth/AtlasProtected/PhotonID

Trigger	p_T^ℓ cut
HLT_e60_lhmedium_nod0	
HLT_e140_lhloose_nod0	
HLT_2e24_lhvloose_nod0	$p_T^{e_2} > 26$ GeV
HLT_2e17_lhvloose_nod0_L12EM15VHI[2]	$p_T^{e_2} > 21$ GeV

Table 2: Unprescaled electron triggers

Trigger	p_T^ℓ cut
HLT_mu50	
HLT_2mu14	$p_T^{\mu_2} > 16$ GeV
HLT_mu26_ivarmedium	$p_T^{\mu_1} > 28$ GeV

Table 3: Unprescaled muon triggers

Trigger
HLT_e60_lhmedium_nod0_match
HLT_e140_lhloose_nod0_match
HLT_2e24_lhvloose_nod0_match
HLT_2e17_lhvloose_nod0_L12EM15VHI_match

Table 4: Prescaled electron triggers

Trigger
HLT_mu50_match
HLT_mu50_0eta105_msonly
HLT_mu50_0eta105_msonly_match
HLT_2mu14_match
HLT_mu26_imedium
HLT_mu26_imedium_match
HLT_mu26_ivarmedium_OR_HLT_mu50
HLT_mu26_ivarmedium_OR_HLT_mu50_match
HLT_mu26_ivarmedium
HLT_mu26_ivarmedium_match

Table 5: Prescaled muon triggers

HLT_e26_lhtight_nod0_ivarloose and HLT_mu22_mu8noL1 are unprescaled triggers which are missing from the version 00-02-03 ntuples. This leads to a 10% loss in data.

Figures 3-14 demonstrate the importance of making p_T^ℓ cuts. Although the use of only unprescaled triggers does not noticeably affect the data, the implementation of associated p_T^ℓ cuts significantly improves the data-MC agreement for $p_T^{\mu_1} < 20$ GeV, $p_T^{\mu_2} < 20$ GeV, $p_T^{\ell_1} < 40$ GeV and $p_T^{\ell_2} \approx 20$ GeV. Therefore the use of these cuts improves the quality of subsequent fits and increases the visibility of other inconsistencies between data and MC.

[2]Accidentally prescaled in periods B5-B8 (runs 326834-328393 with an effective reduction of 0.6 fb^{-1}) but was used anyway to avoid loss of statistical power

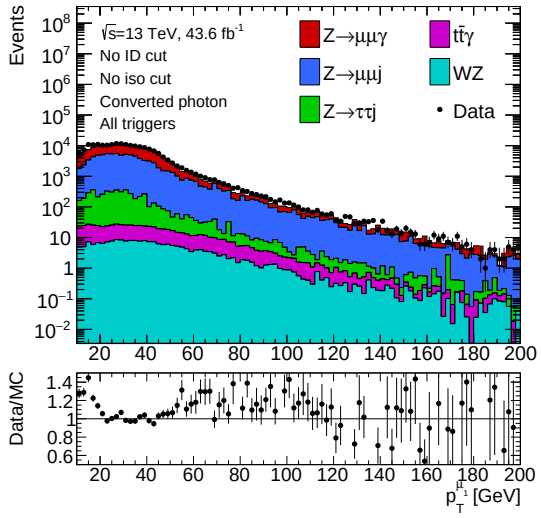

Figure 3: p_T^ℓ distribution of the leading muon in events with a converted photon. Events passing any trigger saved in the ntuples are used and no p_T^ℓ cuts are applied. No ID or isolation cuts are applied to the photon.

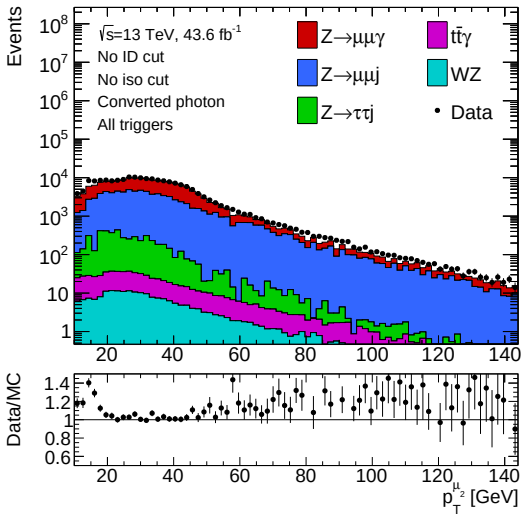

Figure 4: p_T^ℓ distribution of the subleading muon in events with a converted photon. Events passing any trigger saved in the ntuples are used and no p_T^ℓ cuts are applied. No ID or isolation cuts are applied to the photon.

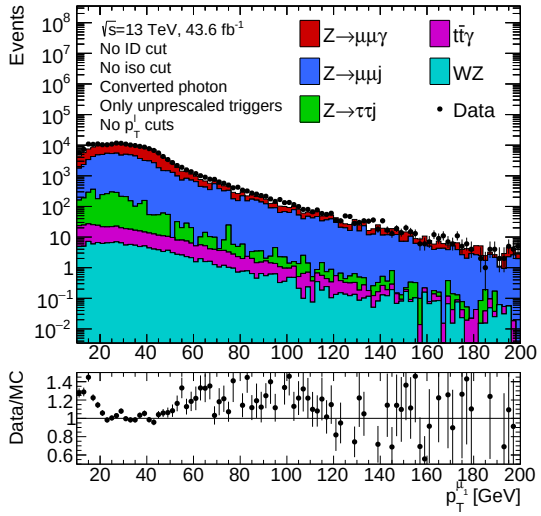

Figure 5: p_T^ℓ distribution of the leading muon in events with a converted photon. Only events passing an unprescaled trigger saved in the ntuples are used but no p_T^ℓ cuts are applied. No ID or isolation cuts are applied to the photon.

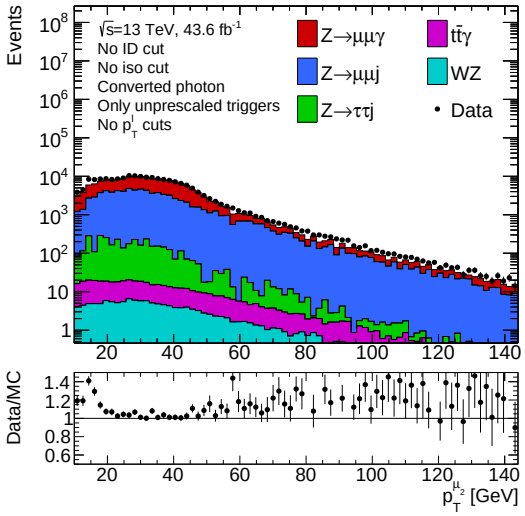

Figure 6: p_T^ℓ distribution of the subleading muon in events with an unconverted photon. Only events passing an unprescaled triggers saved in the ntuples are used but no p_T^ℓ cuts are applied. No ID or isolation cuts are applied to the photon.

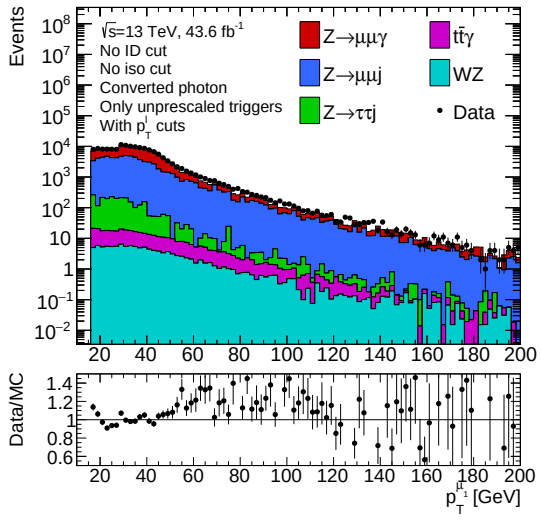

Figure 7: p_T^ℓ distribution of the leading muon in events with an unconverted photon. Only events passing an unprescaled trigger saved in the ntuples are used and p_T^ℓ cuts are applied. No ID or isolation cuts are applied to the photon.

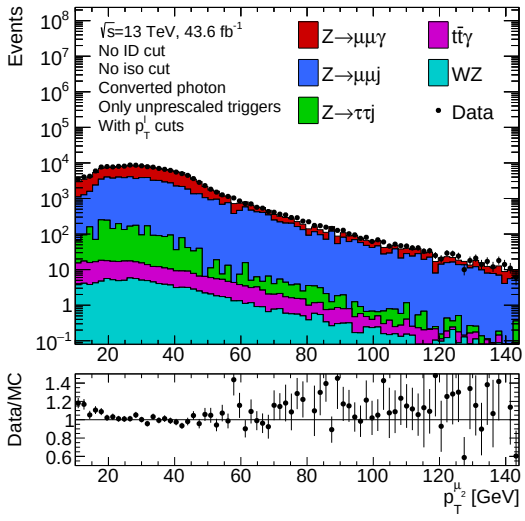

Figure 8: p_T^ℓ distribution of the subleading muon in events with an unconverted photon. Only events passing an unprescaled trigger saved in the ntuple are used and p_T^ℓ cuts are applied. No ID or isolation cuts are applied to the photon.

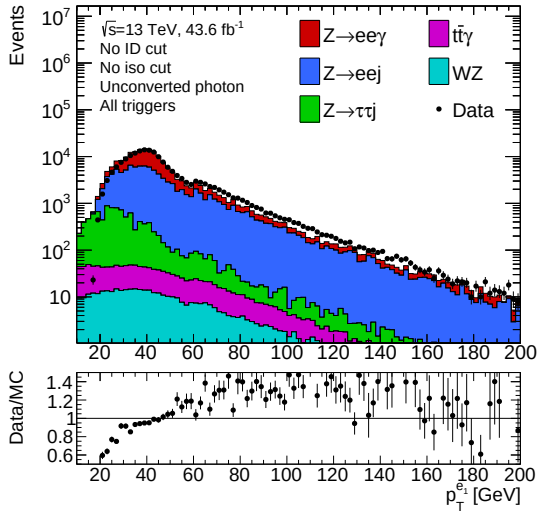

Figure 9: p_T^ℓ distribution of the leading electron in events with an unconverted photon. Events passing any trigger saved in the ntuples are used and no p_T^ℓ cuts are applied. No ID or isolation cuts are applied to the photon.

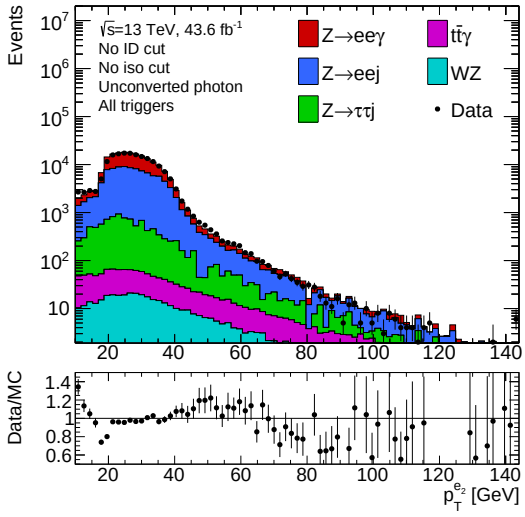

Figure 10: p_T^ℓ distribution of the subleading electron in events with an unconverted photon. Events passing any trigger saved in the ntuples are used and no p_T^ℓ cuts are applied. No ID or isolation cuts are applied to the photon.

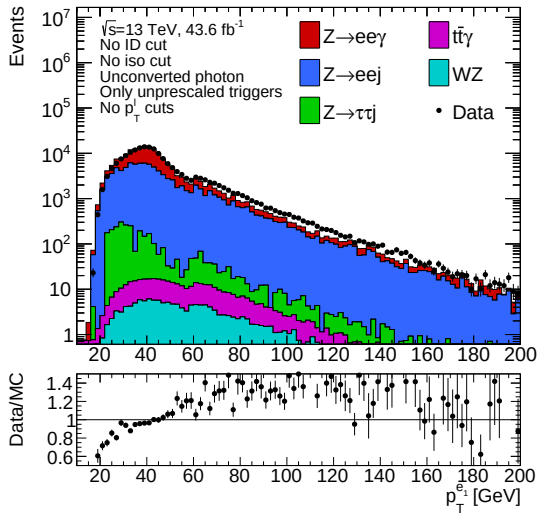

Figure 11: p_T^ℓ distribution of the leading electron in events with an unconverted photon. Only events passing an unprescaled trigger saved in the ntuples are used but no p_T^ℓ cuts are applied. No ID or isolation cuts are applied to the photon.

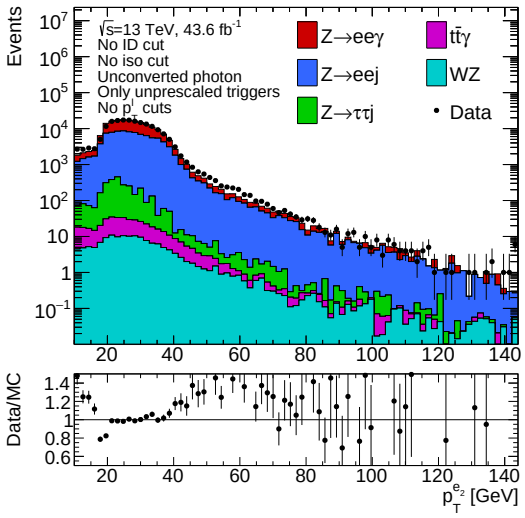

Figure 12: p_T^ℓ distribution of the subleading electron in events with an unconverted photon. Only events passing an unprescaled triggers saved in the ntuples are used but no p_T^ℓ cuts are applied. No ID or isolation cuts are applied to the photon.

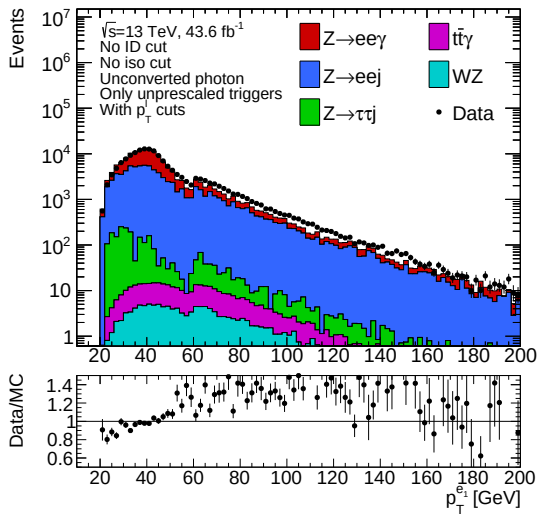

Figure 13: p_T^ℓ distribution of the leading electron in events with an unconverted photon. Only events passing an unprescaled trigger saved in the ntuples are used and p_T^ℓ cuts are applied. No ID or isolation cuts are applied to the photon.

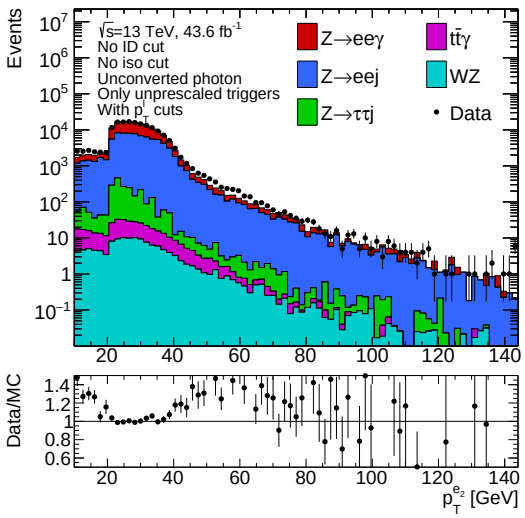

Figure 14: p_T^ℓ distribution of the subleading electron in events with an unconverted photon. Only events passing an unprescaled trigger saved in the ntuple are used and p_T^ℓ cuts are applied. No ID or isolation cuts are applied to the photon.

4 ID and isolation criteria

In all cases, the tight ID criteria are used to define ID cuts. Isolated photons are those that pass the FixedCutLoose working point:

$$E_T^{cone20}/p_T < 0.065 \tag{2}$$

$$p_T^{cone20}/p_T < 0.050 \tag{3}$$

where E_T^{cone20}/p_T measures the calorimeter isolation and p_T^{cone20}/p_T the track isolation.

To effectively exclude signal, the anti-isolation region is much tighter than the inverse of the isolation region. It also has an upper limit to avoid biasing the $m_{\ell\ell\gamma}$ shape:

$$0.20 < E_T^{cone20}/p_T < 1.00 \tag{4}$$

$$0.15 < p_T^{cone20}/p_T < 1.00 \tag{5}$$

5 Backgrounds

Figure 15 shows the p_T^γ distribution of the signal channel and all backgrounds, compared to the distribution of data events. $Z \to \ell\ell j$ is a significant background everywhere. $Z \to \tau\tau j$ may be significant at $p_T^\gamma < 40$ GeV. $t\bar{t}\gamma$ and WZ are small everywhere, but are most significant at $p_T^\gamma > 60$ GeV.

The method described in this report treats reducible and irreducible backgrounds differently. Reducible backgrounds are those that contain a fake or non-isolated photon, so can be reduced by making an isolation or ID cut. The reducible backgrounds here are $Z \to \ell\ell j$ and $Z \to \tau\tau j$. $t\bar{t}\gamma$ is an irreducible background. WZ is treated as an irreducible background, although it does not fall into either category.

There is a significant discrepancy between data and MC at $p_T^\gamma \approx 10$ GeV. This suggests that a background channel is missing from the MC description. This is discussed further in section 9.2.

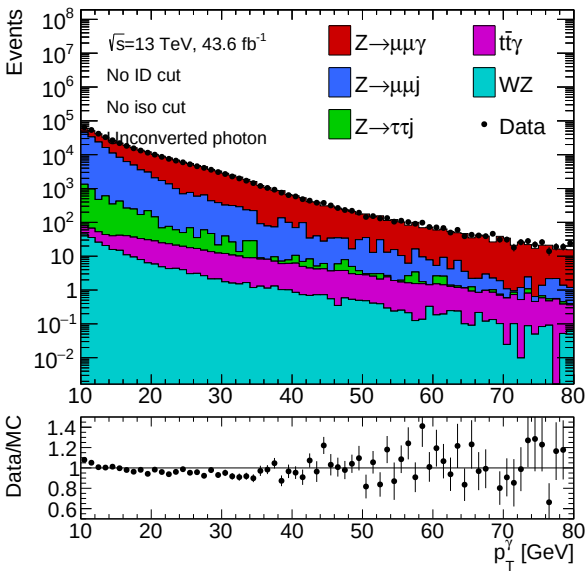

Figure 15: p_T^γ distribution of events with muons and an unconverted photon which satisfy selection cuts (markers). The signal is $Z \to \mu\mu\gamma$ (red) and the dominant background is $Z \to \mu\mu j$ (dark blue). The next largest background is $Z \to \tau\tau j$ (green), which is mainly in the region $p_T^\gamma < 40$ GeV. $t\bar{t}\gamma$ (pink) and WZ (light blue) are small everywhere. Agreement between data and Monte Carlo is generally good but there is a deficit of Monte Carlo compared to data at $p_T^\gamma \approx 10$ GeV.

Table 6 provides estimates on the maximum fractional errors on ϵ_{ID} and ϵ_{TOT} as a result of ignoring backgrounds. These were evaluated by calculating $\Delta\epsilon$ when the number of signal events N_s was increased by the number of background events, in the p_T^γ bin with the highest fraction of background. This demonstrates that $Z \to \tau\tau j$ is significant and so must be accurately modelled, whereas $t\bar{t}\gamma$ and WZ do not need to be modelled as accurately.

	$\tau\tau j$	$t\bar{t}\gamma$	WZ
$\Delta\epsilon_{ID}/\epsilon_{ID}$	0.4%	0.03%	0.01%
$\Delta\epsilon_{TOT}/\epsilon_{TOT}$	2%	0.3%	0.05%
Bin	$10 < p_T^\gamma < 15$ GeV	$60 < p_T^\gamma < 80$ GeV	

Table 6: Estimate of the maximum fractional error on ϵ_{ID} and ϵ_{TOT} as a result of ignoring the backgrounds $Z \to \tau\tau j$, $t\bar{t}\gamma$ and WZ.

6 Method

Efficiencies are calculated using the events which pass the selection criteria in section 3. Photon tight identification efficiency ϵ_{ID} is the fraction of isolated photons which pass the tight identification criteria:

$$\epsilon_{ID} = \frac{N_S[\text{ID\&iso}]}{N_s[\text{iso}]} \tag{6}$$

Photon total efficiency ϵ_{TOT} is the fraction of photons which pass the tight identification and FixedCutLoose isolation criteria:

$$\epsilon_{TOT} = \frac{N_S[\text{ID\&iso}]}{N_s} \tag{7}$$

Both efficiencies are evaluated in the range $m_{\ell\ell\gamma}$ = [80,100] GeV. The lower bound on this range was chosen because most events outside of this range were a result of mismeasurement, and so were considered low-quality events. Low-quality would not generally be used in analysis, and so the efficiency of only high-quality events was calculated.

Photon efficiencies depend on whether the photon is converted (undergoes e^+e^- pair production before ECAL) or unconverted (undergoes pair production in ECAL); absolute photon pseudorapidity $|\eta^\gamma|$; and p_T^γ, so are calculated separately for converted and unconverted photons, and in the following bins of $|\eta^\gamma|$ and p_T^γ. They are also calculated separately for events with electrons and muons.

$$p_T^\gamma : [10, 15, 20, 25, 30, 35, 40, 45, 50, 60, 80] \quad \text{GeV} \tag{8}$$

$$|\eta^\gamma| : [0.00, 0.60, 1.37, 1.52, 1.81, 2.37] \tag{9}$$

Excluding the range $1.37 < |\eta^\gamma| < 1.52$ due to a lack of detector coverage.

The following sections explain the current method of measuring ϵ_{ID} and the modifications to the method which have been tested.

6.1 Existing method

For $p_T^\gamma < 25$ GeV , background contamination is large and is estimated using a template fit. Only the dominant background $Z \to \ell\ell j$ is considered. Templates for signal and background are taken from Monte Carlo and fitted to the data distribution to obtain the purity (P). The efficiency is then evaluated as:

$$\epsilon = \frac{P_{cut} \times N_{data,cut}}{P \times N_{data}} \tag{10}$$

For $p_T^\gamma > 25$ GeV, the background contamination is small and is not evaluated. Instead, the effect of contamination is treated as a systematic uncertainty on ϵ.

For more detail, see [1, 9, 6].

6.2 Reducible background template

The reducible background template is now taken from data in an anti-isolation, anti-ID control region (CR, see section 4 for definition), rather than from Monte Carlo in the signal region. Figures 16 and 17 show the calorimeter and track isolation distribution of all channels. This demonstrates that almost all signal events have calorimeter isolation < 0.3 and track isolation < 0.2. The CR is looser than the inversion of this region to maintain high available statistics. This produces a data set with a large number of reducible background events and only a small fraction (up to 1%) of signal and irreducible background contamination.

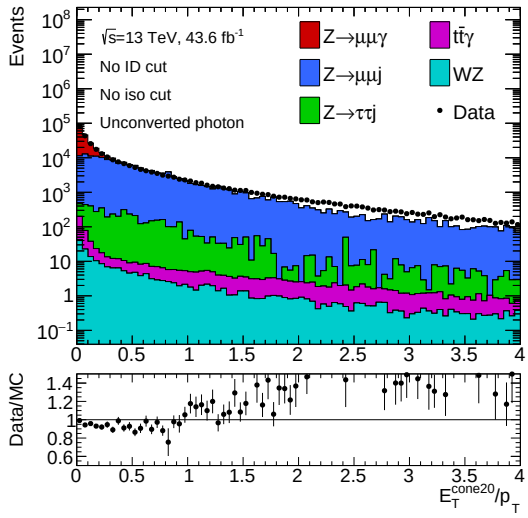

Figure 16: Calorimeter isolation E_T^{cone20}/p_T^γ distribution of events with muons and an unconverted photon. The number of signal events rapidly decreases, so there are almost none with $E_T^{cone20}/p_T^\gamma > 0.3$. The number of reducible background events decreases slowly with respect to isolation but is large everywhere. Data-MC agreement is much worse at high E_T^{cone20}/p_T^γ.

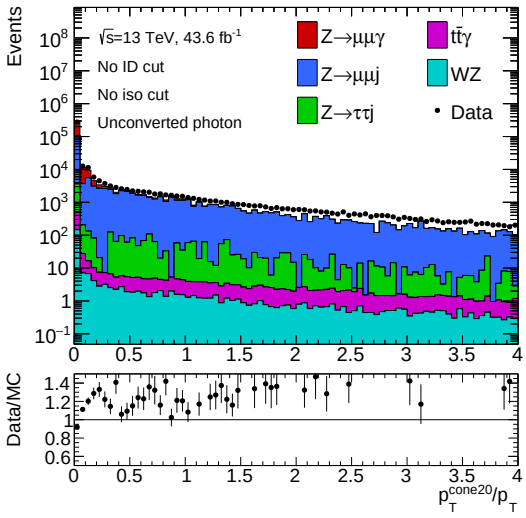

Figure 17: Track isolation p_T^{cone20}/p_T^γ distribution of events with muons and an unconverted photon. The number of signal events rapidly decreases, so there are almost none with $p_T^{cone20}/p_T^\gamma > 0.2$. The number of reducible background events decreases slowly with respect to isolation but is large everywhere. Data-MC agreement is much worse at high p_T^{cone20}/p_T^γ.

The use of an anti-isolation control region relies on the $m_{\ell\ell\gamma}$ distribution being independent of isolation. Figure 18 compares the agreement in shape between CR data and MC (with no cuts) in four different parts of the control region. It shows that the $m_{\ell\ell\gamma}$ distribution of the background is not independent of isolation: As the photons become less isolated (E_T^{cone20}/p_T^γ and p_T^{cone20}/p_T^γ increase), the distribution becomes more skewed towards large $m_{\ell\ell\gamma}$. This indicates that it is necessary to exlcude events with $E_T^{cone20}/p_T^\gamma > 1.00$ or $p_T^{cone20}/p_T^\gamma > 1.00$ in the background template, as this would bias the shape. Therefore these values are chosen as the upper bound on the control region.

Comparisons in all bins are shown in the supplementary appendix. Due to low available statistics, it is difficult to determine if there is a bias at $p_T^\gamma > 20$ GeV. If there is no bias, it may be possible to increase the upper bound on the control region for $p_T^\gamma > 20$ GeV, which would improve the statistical power of the reducible background template.

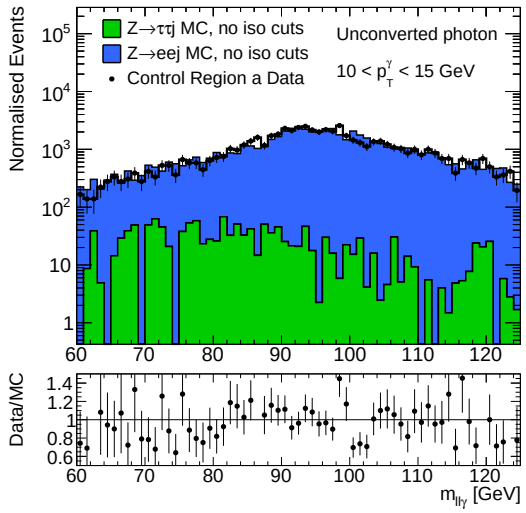

(a) Comparison using control region a: $0.20 < E_T^{cone20}/p_T^\gamma < 0.50$ & $0.15 < p_T^{cone20}/p_T^\gamma < 0.50$. There is good agreement between the distributions.

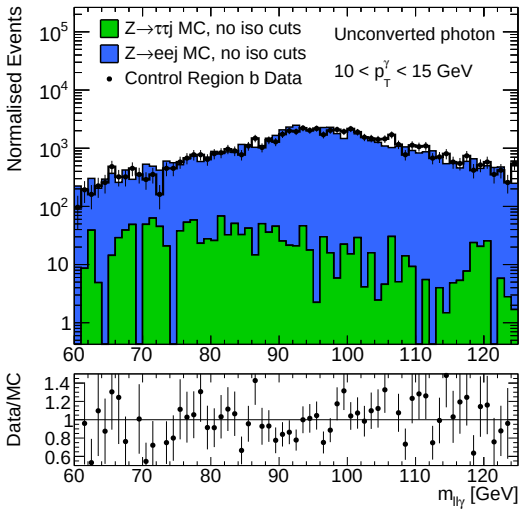

(b) Comparison using control region b: $0.50 < E_T^{cone20}/p_T^\gamma < 1.00$ & $0.50 < p_T^{cone20}/p_T^\gamma < 1.00$. There is good agreement between the distributions.

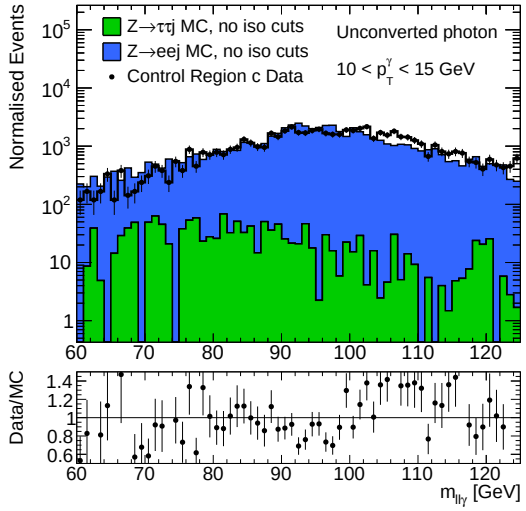

(c) Comparison using control region c: $1.00 < E_T^{cone20}/p_T^\gamma < 2.00$ & $1.00 < p_T^{cone20}/p_T^\gamma < 2.00$. The CR data distribution is slightly more skewed towards large $m_{\ell\ell\gamma}$ than the MC distribution.

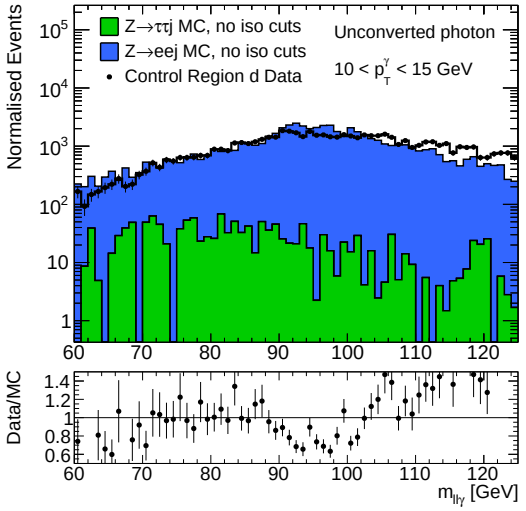

(d) Comparison using control region d: $2.00 < E_T^{cone20}/p_T^\gamma$ & $2.00 < p_T^{cone20}/p_T^\gamma$. The CR data distribution is significantly more skewed towards large $m_{\ell\ell\gamma}$ than the MC distribution.

Figure 18: Comparison of $m_{\ell\ell\gamma}$ distribution between data in control region (markers) and reducible background MC with no isolation cuts (blue+green), for background to $Z \to ee\gamma$ with an unconverted photon. Skew towards large $m_{\ell\ell\gamma}$ increases as photons become less isolated (from CRa to CRd).

Figure 19 compares the reducible background templates when using data from the selected CR (section 4) and Monte Carlo (with no isolation or ID cuts), for background to $Z \to \mu\mu\gamma$ with a converted photon. The template shapes are consistent in all cases. At $p_T^\gamma < 20$ GeV, both templates have good statistics. At $20 < p_T^\gamma < 40$ GeV, the CR data template has better

statistics than the MC, but above this, its statistical power decreases significantly, particularly for $m_{\ell\ell\gamma} < 80$ GeV.

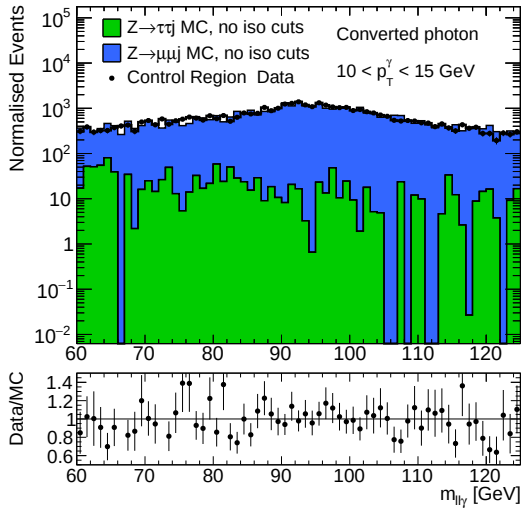

(a) Comparison in the bin $10 < p_T^\gamma < 15$ GeV. Both CR data and MC have good statistics.

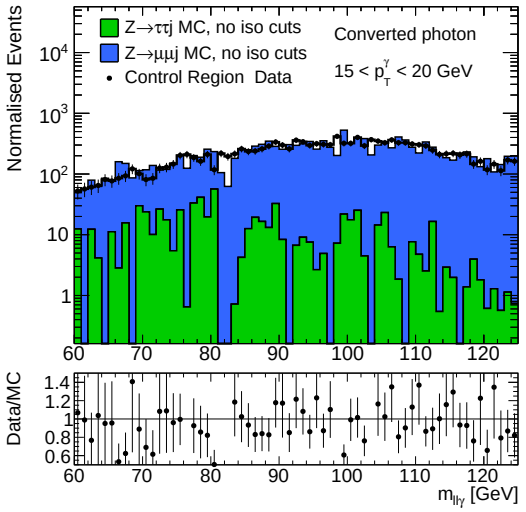

(b) Comparison in the bin $15 < p_T^\gamma < 20$ GeV. Both CR data and MC have good statistics.

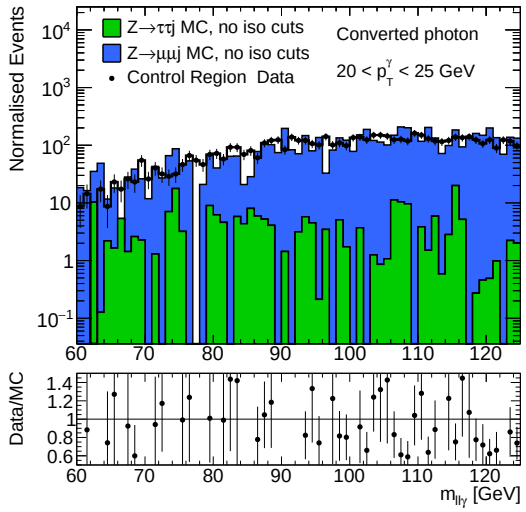

(c) Comparison in the bin $20 < p_T^\gamma < 25$ GeV. The CR data template has better statistical power than the MC.

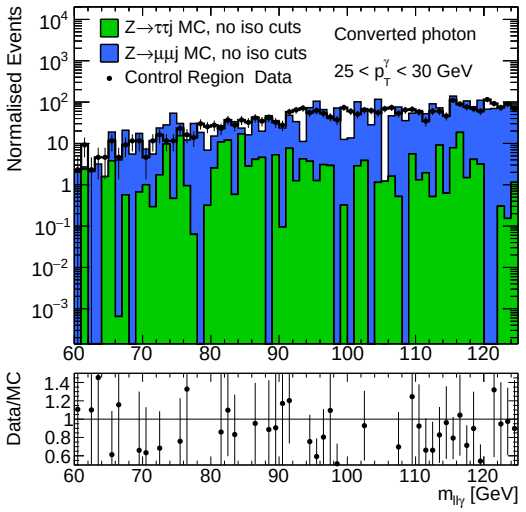

(d) Comparison in the bin $25 < p_T^\gamma < 30$ GeV. The CR data template has better statistical power than the MC.

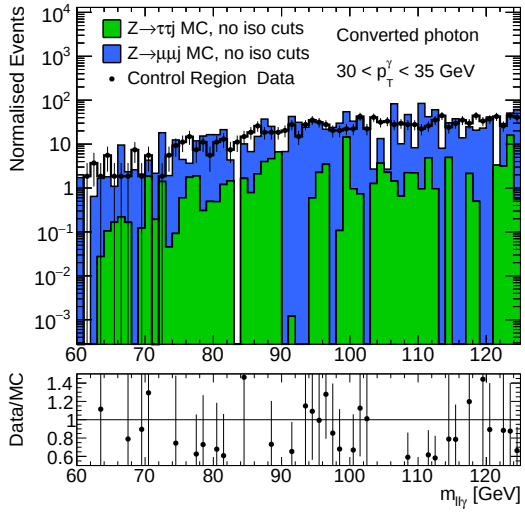

(e) Comparison in the bin $30 < p_T^\gamma < 35$ GeV. The CR data template has better statistical power than the MC.

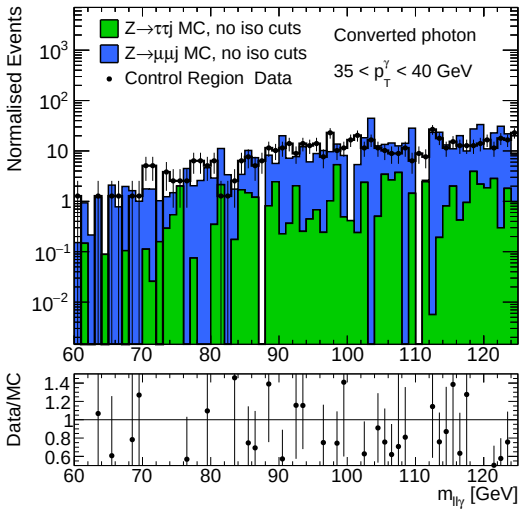

(f) Comparison in the bin $35 < p_T^\gamma < 40$ GeV. The CR data template has better statistical power than the MC.

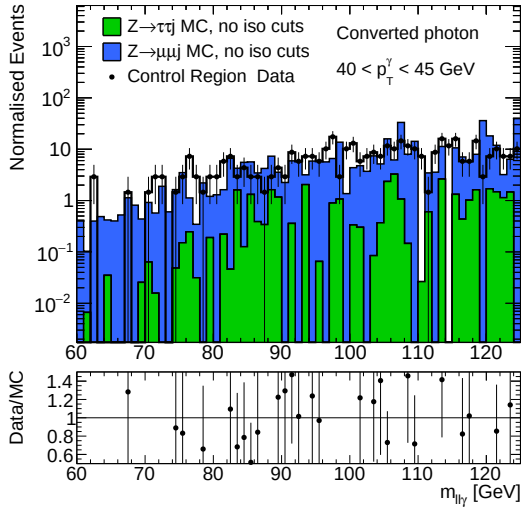

(g) Comparison in the bin $40 < p_T^\gamma < 45$ GeV. The CR data has poor statistical power for $m_{\ell\ell\gamma} < 80$ GeV.

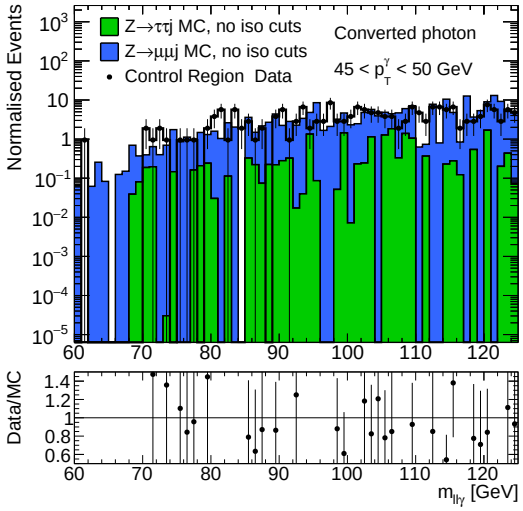

(h) Comparison in the bin $45 < p_T^\gamma < 50$ GeV. The CR data has poor statistical power for $m_{\ell\ell\gamma} < 80$ GeV.

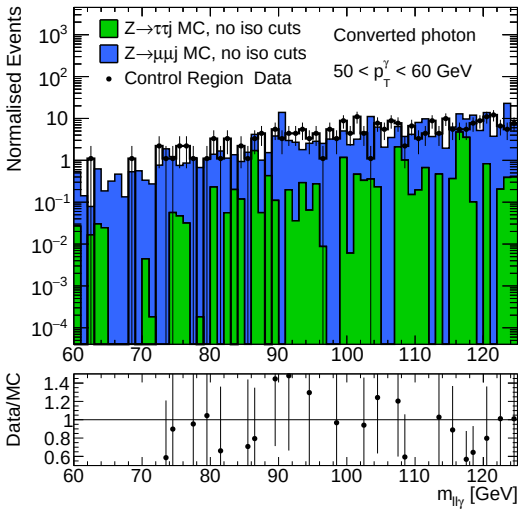

(i) Comparison in the bin $50 < p_T^\gamma < 60$ GeV. The CR data has poor statistical power for $m_{\ell\ell\gamma} < 80$ GeV.

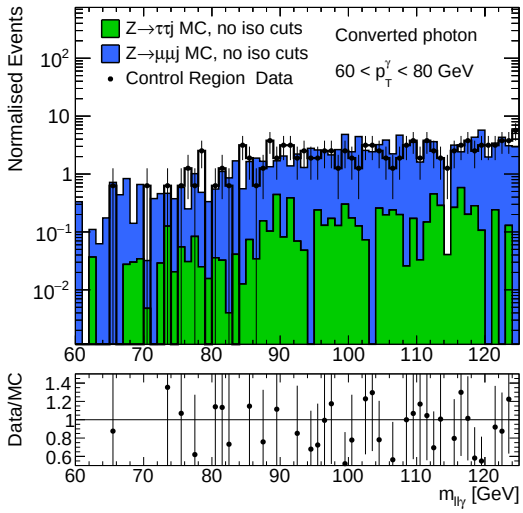

(j) Comparison in the bin $60 < p_T^\gamma < 80$ GeV. The CR data has poor statistical power for $m_{\ell\ell\gamma} < 80$ GeV.

Figure 19: Comparison of $m_{\ell\ell\gamma}$ distribution between data in control region (markers) and reducible background MC with no isolation cuts (blue+green), for background to $Z \to \mu\mu\gamma$ with an unconverted photon. There is agreement between the two templates at all p_T^γ.

To further improve the statistical power of the background template, all $|\eta^\gamma|$ bins are used to produce the template. This relies on the $m_{\ell\ell\gamma}$ distribution being unbiased with respect to $|\eta^\gamma|$, which is illustrated in figures 20 and 21. These show the ratio between the $m_{\ell\ell\gamma}$ distribution in one bin of $|\eta^\gamma|$ and the $m_{\ell\ell\gamma}$ distribution in all bins of $|\eta^\gamma|$ for two cases. Plots for all cases are provided in the supplementary appendix. The ratio between the two distributions is consistent with a constant value, which demonstrates that the shape of the $m_{\ell\ell\gamma}$ distribution is independent of $|\eta^\gamma|$.

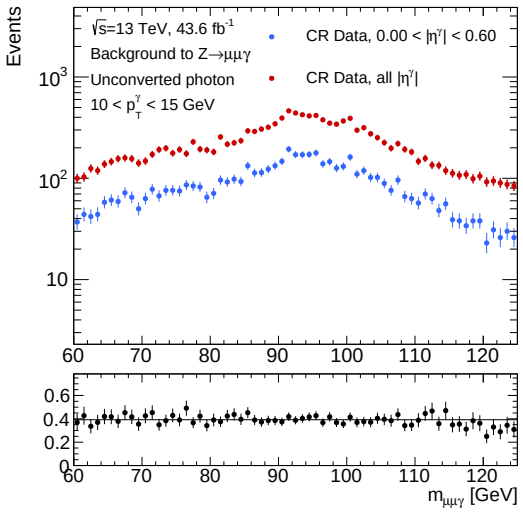

Figure 20: $m_{\ell\ell\gamma}$ distribution of control region events in the range $10 < p_T^\gamma < 15$ GeV which are reducible background to $Z \to \mu\mu\gamma$ with an unconverted photon, in the bin $0.00 < |\eta^\gamma| < 0.60$ (blue markers) and for all $|\eta^\gamma|$ (red markers). The ratio between the two is consistent with a constant value with respect to $m_{\ell\ell\gamma}$.

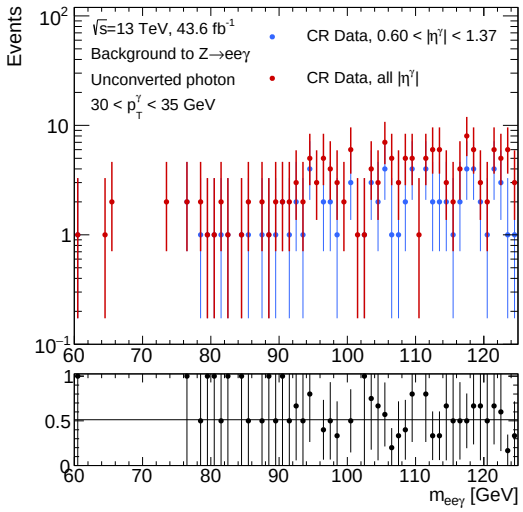

Figure 21: $m_{\ell\ell\gamma}$ distribution of control region events in the range $30 < p_T^\gamma < 35$ GeV which are reducible background to $Z \to ee\gamma$ with an unconverted photon, in the bin $0.60 < |\eta^\gamma| < 1.37$ (blue markers) and for all $|\eta^\gamma|$ (red markers). The ratio between the two is consistent with a constant value with respect to $m_{\ell\ell\gamma}$.

The improvement in statistical power is particularly noticeable in bins with $p_T^\gamma > 25$ GeV, where there are only a small number of MC events. This is illustrated in figure 22.

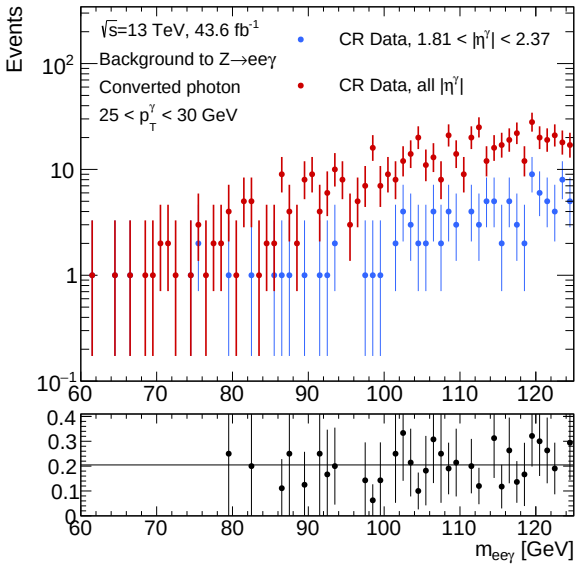

Figure 22: Comparison between $m_{\ell\ell\gamma}$ distribution from CR data in the bin $1.81 < |\eta^\gamma| < 2.37$ (blue) and in all $|\eta^\gamma|$ bins combined (red), for events in the range $25 < p_T^\gamma < 30$ GeV which include electrons and a converted photon. The two data sets have approximately the same shape, but the data set using all $|\eta^\gamma|$ has much better statistics.

Another benefit of using data as a reducible background template is that it includes any reducible bacgkrounds which are missing in the Monte Carlo description of the data.

The CR data is then fitted to a double-sided crystal ball function (DSCB) to reduce statistical fluctuations. This is implemented as an unbinned maximum likelihood fit in RooFit [10]. The fit excludes the range [88,93] GeV to reduce the impact of signal and irreducible background contamination. The DSCB is an asymmetric function with a Gaussian core and power-law tails (figure 23).

Figures 24 and 25 illustrate the fit in two bins. The fits for all bins are shown in the supplementary appendix.

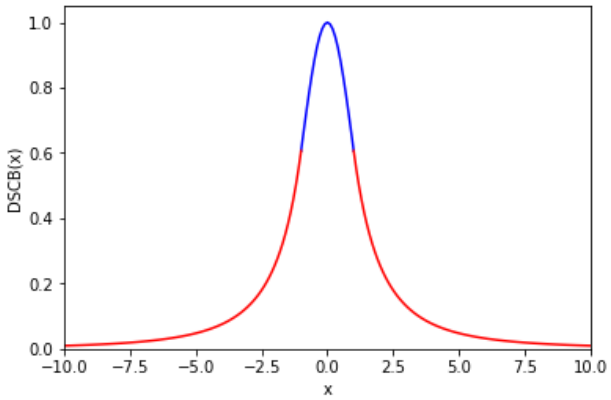

Figure 23: Plot of a double-sided crystal ball function. The core is Gaussian (blue) and the tails follow a power law (red).

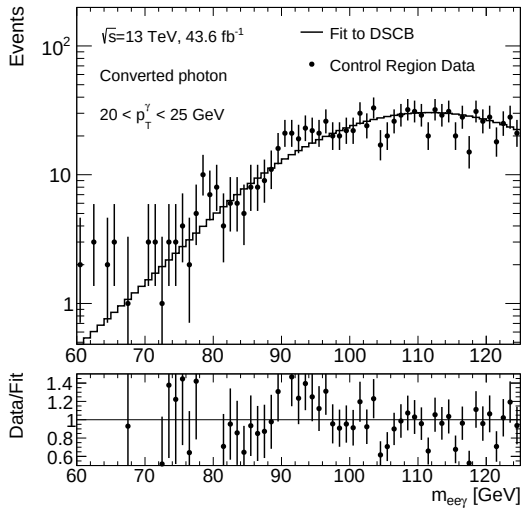

Figure 24: Fit of a DSCB to the $m_{\ell\ell\gamma}$ distribution of the CR data in the $20 < p_T^\gamma < 25$ GeV, electrons and converted photon bin.

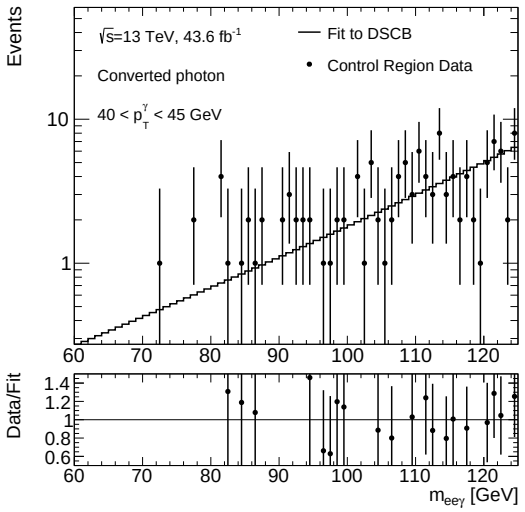

Figure 25: Fit of a DSCB to the $m_{\ell\ell\gamma}$ distribution of the CR data in the $40 < p_T^\gamma < 45$ GeV, electrons and converted photon bin.

6.3 Efficiency Measurement

An extended maximum likelihood fit is implemented in RooFit [10] to fit the signal and background templates to data to determine the number of signal events. The signal and irreducible background templates are taken from Monte Carlo. The irreducible background is treated as a fixed template, so its scaling is not allowed to vary from the value $\sigma_{data}/\sigma_{MC}$. This is 1 for $t\bar{t}\gamma$ and 1.18 for WZ [7]. $|\eta^\gamma|$ bins are also grouped in this fit to increase statistical power.

The fit is carried out in the range $m_{\ell\ell\gamma}$ = [60,125] GeV to utilise the sidebands to accurately determine the size of the background component. The upper limit on this range was set by the upper limit of $m_{\ell\ell\gamma}$ in the data and Monte Carlo samples. The lower limit was selected due to the presence of a kinematic edge at $m_{\ell\ell\gamma} \approx 58$ GeV.

Once the number of signal events before and after a cut had been obtained, the efficiency was calculated in the range $m_{\ell\ell\gamma}$ = [80,100] GeV.

7 Uncertainties

7.1 Statistical

Statistical uncertainties were evaluated using the binomial approximation where N_s has the Poissonian uncertainty $\sqrt{N_s}$. This leads to the uncertainty

$$\Delta\epsilon = \frac{\sqrt{\epsilon(1-\epsilon)}}{N_S} \tag{11}$$

However, this is not a good approximation for $\epsilon \approx 1$ [2].

This leads to statistical uncertainties of up to 1% for $p_T^\gamma < 20$ GeV and up to 5% for $p_T^\gamma > 60$ GeV.

7.2 Background modelling

A systematic uncertainty arises due to inaccurate modelling of the background shape. This is due to a poor fit of the DSCB to the CR data, primarily at $p_T^\gamma < 20GeV$ and $p_T^\gamma > 50$

GeV; dependence of the background shape on isolation; and missing irreducible backgrounds. This uncertainty could be estimated by performing a high and low-tail fit of the signal and background templates to data.

7.3 Detector geometry

Mismodelling of detector geometry in MC leads to a systematic uncertainty. This uncertainty is estimated by evaluating the change in efficiency when an MC sample generated using distorted geometry is used. The maximum fractional uncertainty is 7% and is assumed to be negligible for $p_T^\gamma > 25$ GeV [9].

7.4 Irreducible background cross section

Inaccuracies in the scaling factor $\sigma_{data}/\sigma_{MC}$ of the irreducible backgrounds affect the fit to determine N_S. This uncertainty would be extremely small as the irreducible backgrounds constitute $< 1\%$ of the signal region. It could be estimated by varying the scaling factors within their uncertainties.

8 Results

This section presents measurements of ϵ_{ID} and ϵ_{TOT} in all bins. Measured efficiencies approximately show the expected smooth, monotonic curve with higher efficiencies at higher p_T^γ. There is agreement between data and Monte Carlo in most cases. Systematic errors would need to be evaluated to fully determine the extent of the agreement.

8.1 ID Efficiency Measurements

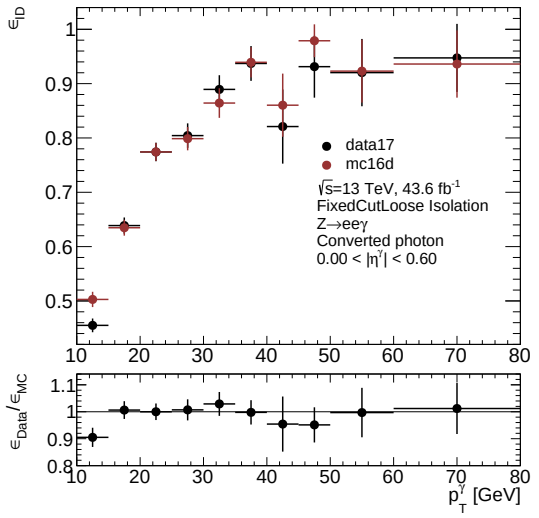

(a) $0.0 < |\eta^{\gamma}| < 0.6$

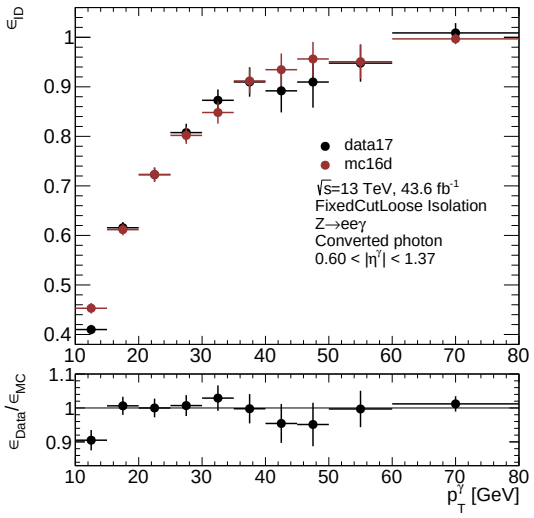

(b) $0.6 < |\eta^{\gamma}| < 1.37$

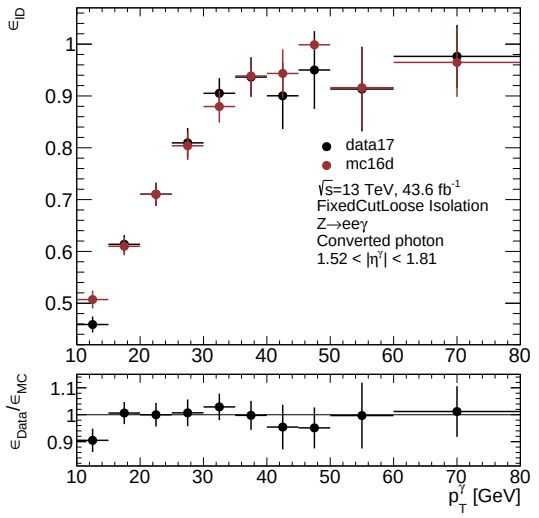

(c) $1.52 < |\eta^{\gamma}| < 1.81$

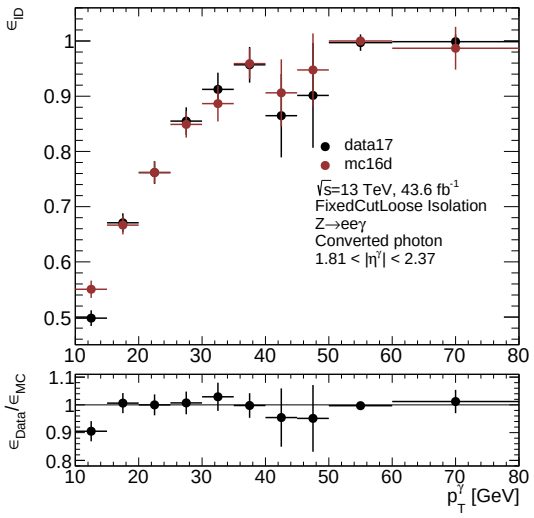

(d) $1.81 < |\eta^{\gamma}| < 2.37$

Figure 26: Comparison of data-driven and MC ID efficiency measurements for events with electrons and a converted photon as a function of p_T^{γ}, for the four pseudorapidity bins. The error bars show statistical uncertainty only.

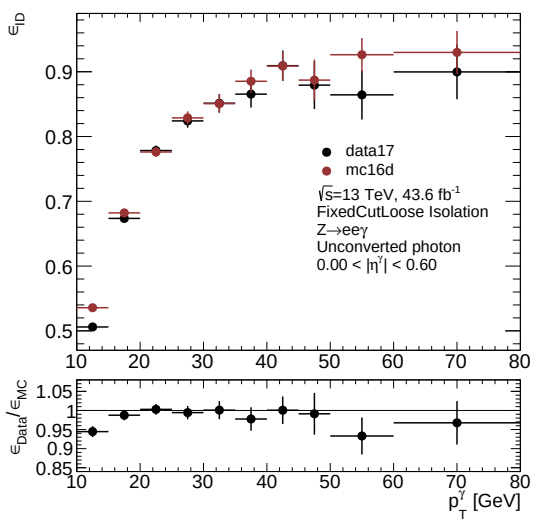

(a) $0.0 < |\eta^{\gamma}| < 0.6$

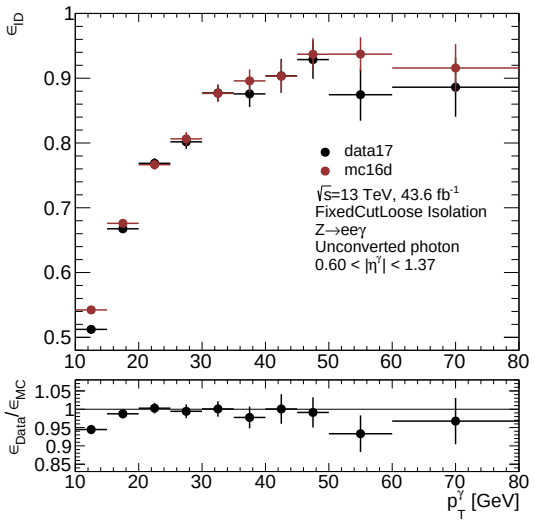

(b) $0.6 < |\eta^{\gamma}| < 1.37$

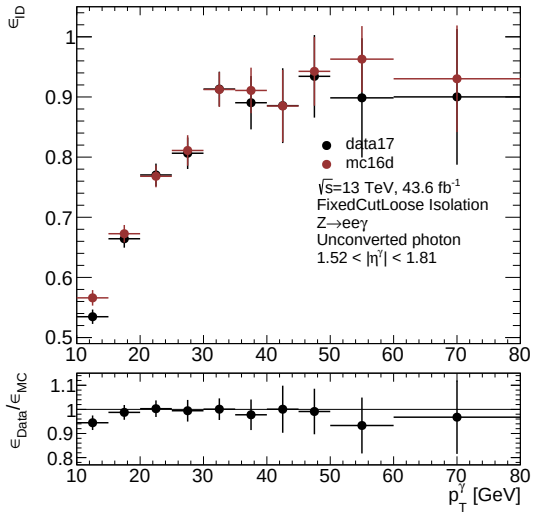

(c) $1.52 < |\eta^{\gamma}| < 1.81$

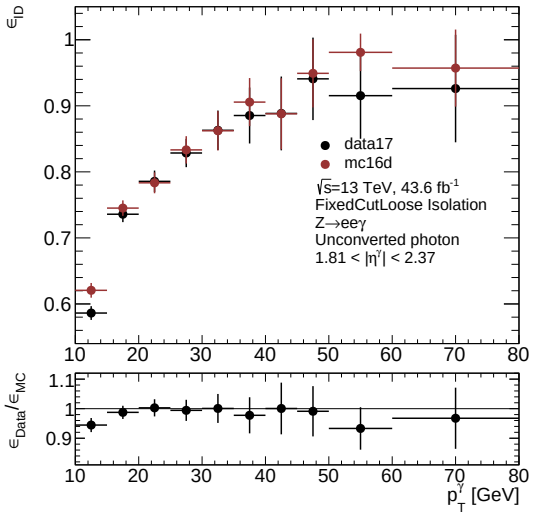

(d) $1.81 < |\eta^{\gamma}| < 2.37$

Figure 27: Comparison of data-driven and MC ID efficiency measurements for events with electrons and an unconverted photon as a function of p_T^{γ}, for the four pseudorapidity bins. The error bars show statistical uncertainty only.

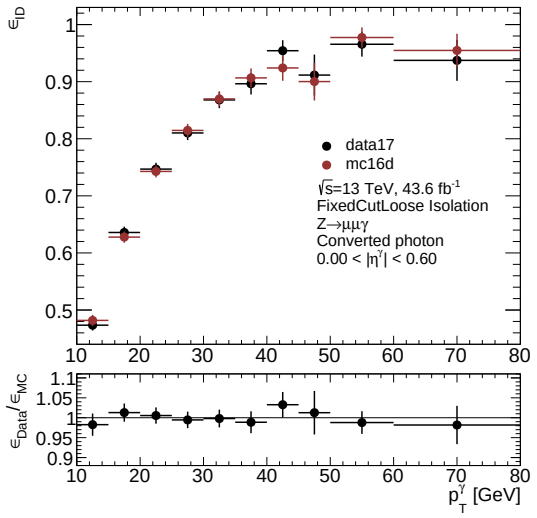

(a) $0.0 < |\eta^{\gamma}| < 0.6$

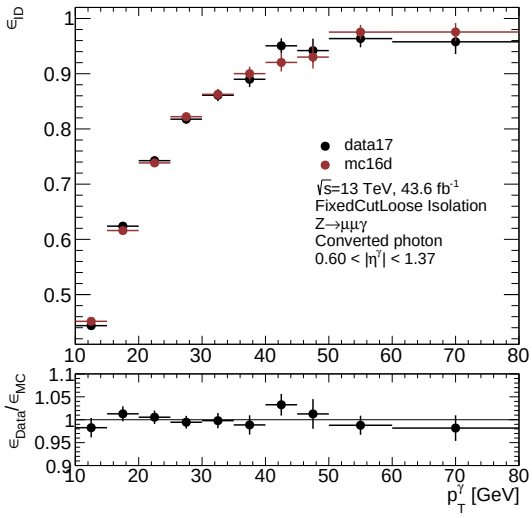

(b) $0.6 < |\eta^{\gamma}| < 1.37$

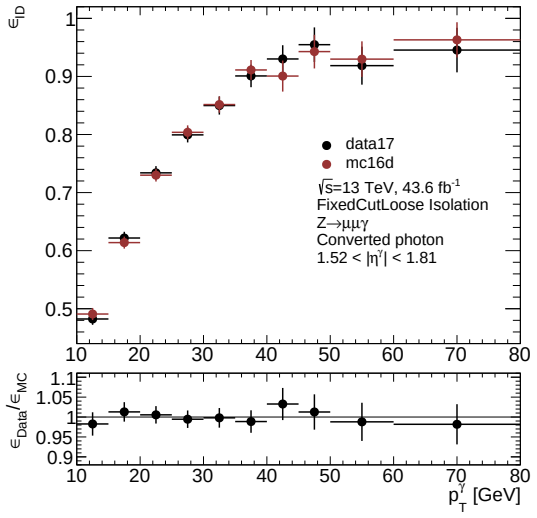

(c) $1.52 < |\eta^{\gamma}| < 1.81$

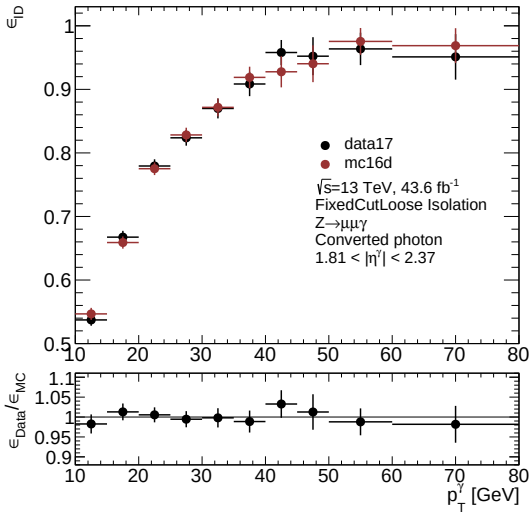

(d) $1.81 < |\eta^{\gamma}| < 2.37$

Figure 28: Comparison of data-driven and MC ID efficiency measurements for events with muons and a converted photon as a function of p_T^{γ}, for the four pseudorapidity bins. The error bars show statistical uncertainty only.

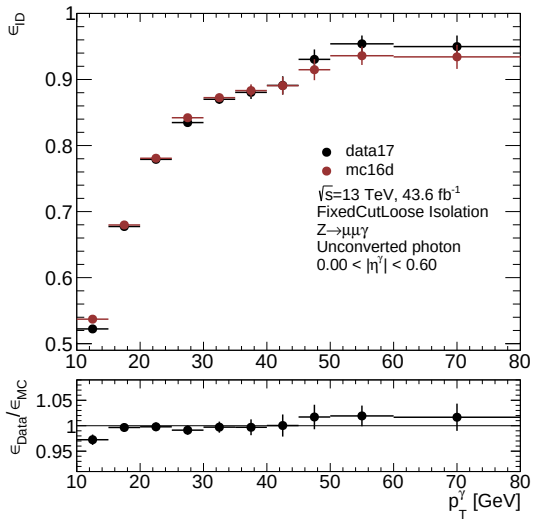

(a) $0.0 < |\eta^{\gamma}| < 0.6$

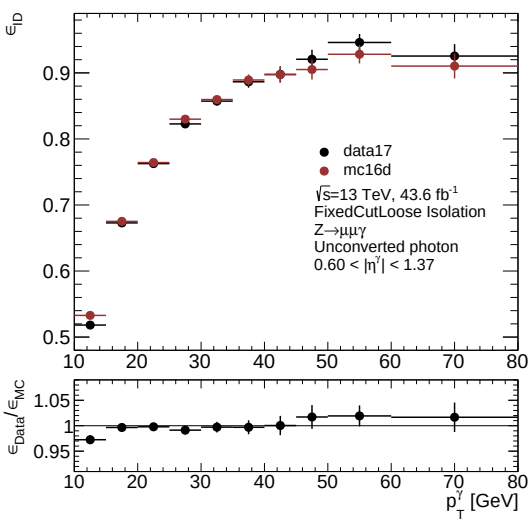

(b) $0.6 < |\eta^{\gamma}| < 1.37$

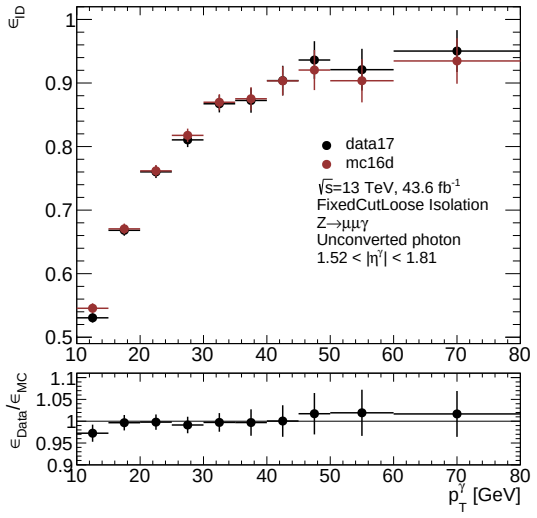

(c) $1.52 < |\eta^{\gamma}| < 1.81$

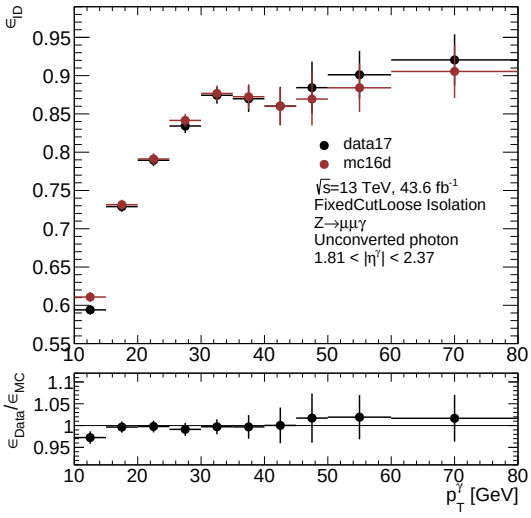

(d) $1.81 < |\eta^{\gamma}| < 2.37$

Figure 29: Comparison of data-driven and MC ID efficiency measurements for events with muons and an unconverted photon as a function of p_T^{γ}, for the four pseudorapidity bins. The error bars show statistical uncertainty only.

8.2 Total Efficiency Measurements

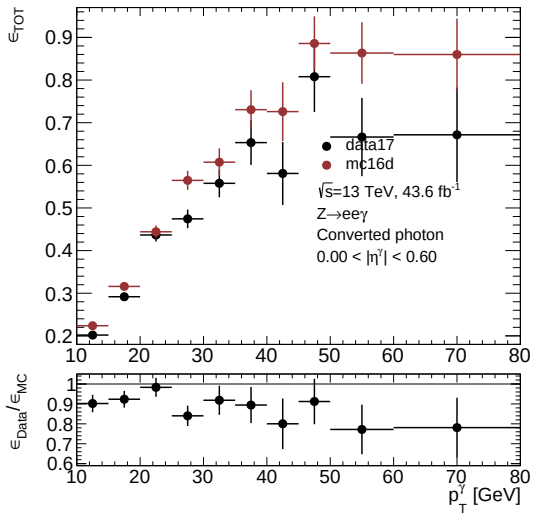

(a) $0.0 < |\eta^{\gamma}| < 0.6$

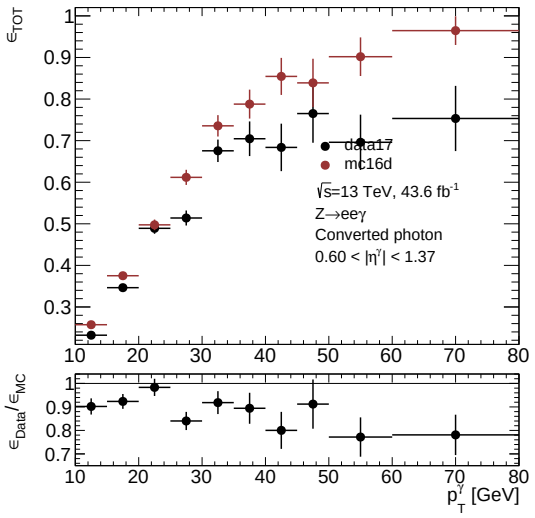

(b) $0.6 < |\eta^{\gamma}| < 1.37$

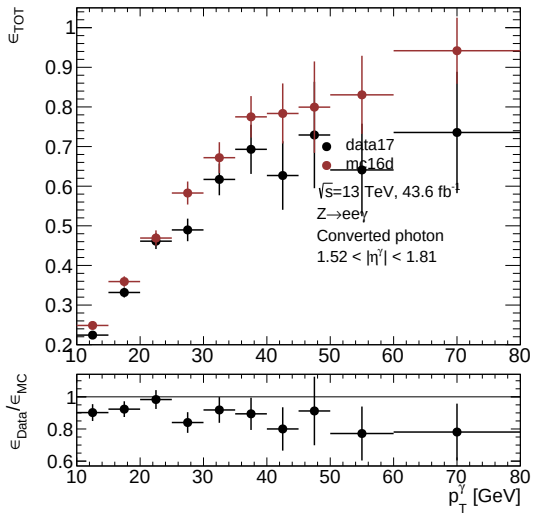

(c) $1.52 < |\eta^{\gamma}| < 1.81$

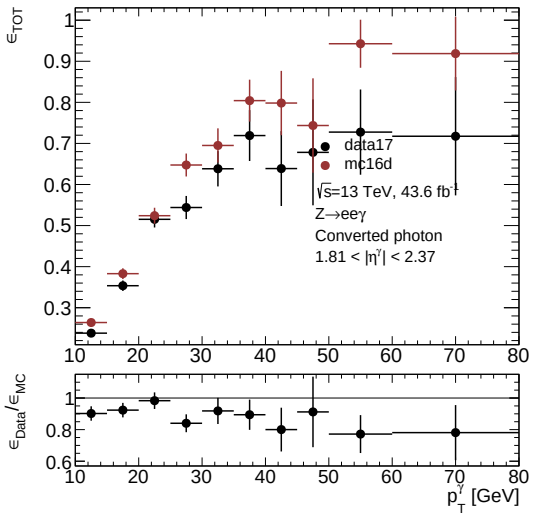

(d) $1.81 < |\eta^{\gamma}| < 2.37$

Figure 30: Comparison of data-driven and MC total efficiency measurements for events with electrons and a converted photon as a function of p_T^{γ}, for the four pseudorapidity bins. The error bars show statistical uncertainty only.

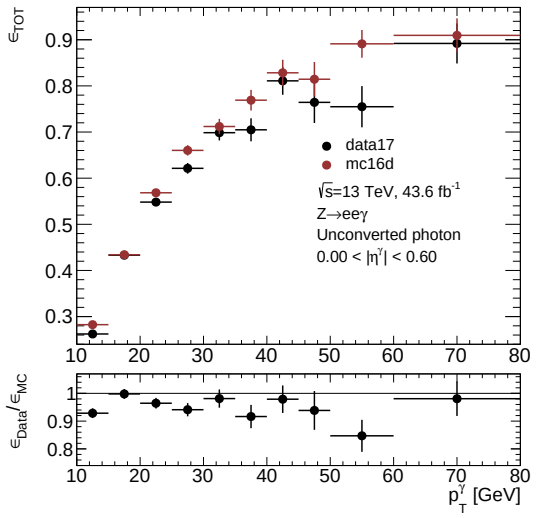

(a) $0.0 < |\eta^{\gamma}| < 0.6$

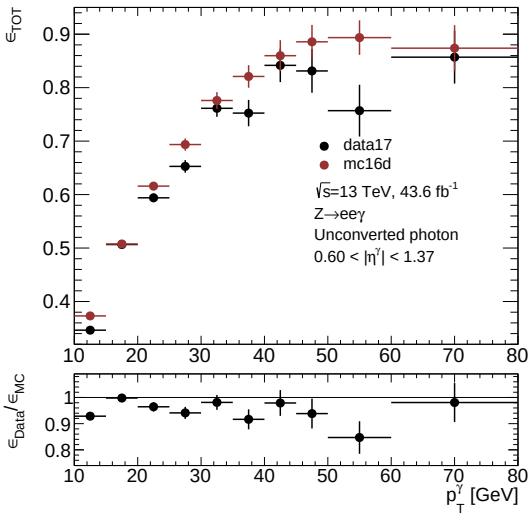

(b) $0.6 < |\eta^{\gamma}| < 1.37$

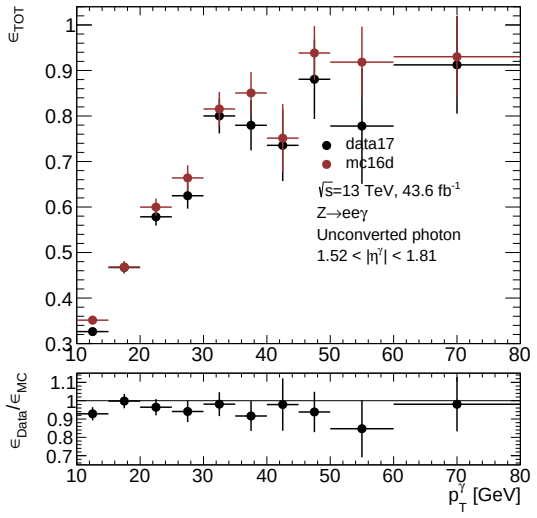

(c) $1.52 < |\eta^{\gamma}| < 1.81$

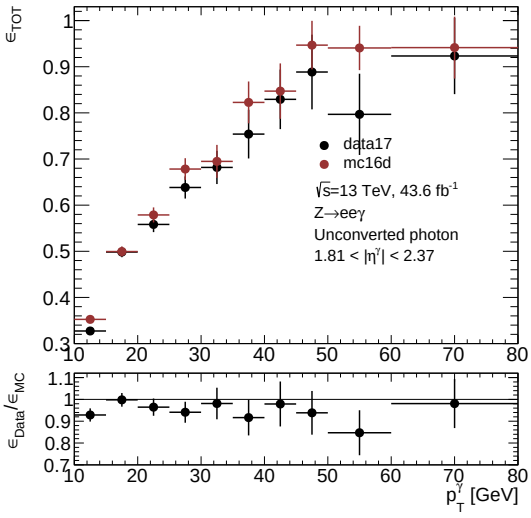

(d) $1.81 < |\eta^{\gamma}| < 2.37$

Figure 31: Comparison of data-driven and MC total efficiency measurements for events with electrons and an unconverted photon as a function of p_T^{γ}, for the four pseudorapidity bins. The error bars show statistical uncertainty only.

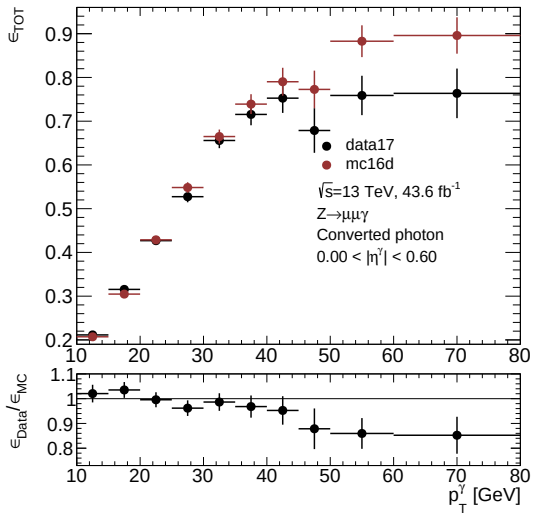

(a) $0.0 < |\eta^{\gamma}| < 0.6$

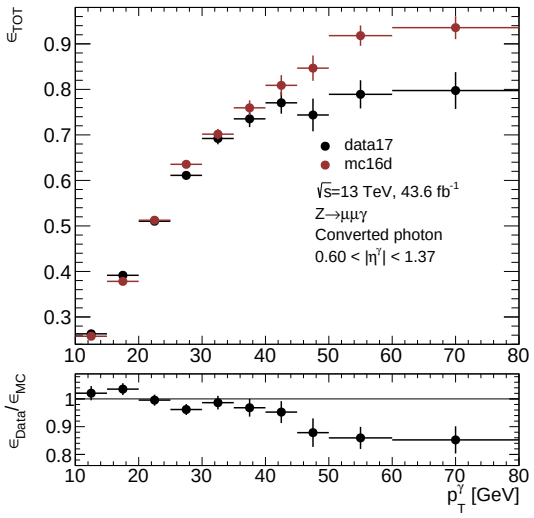

(b) $0.6 < |\eta^{\gamma}| < 1.37$

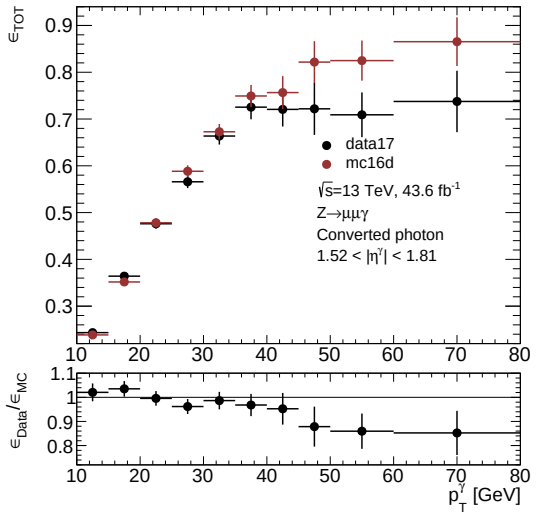

(c) $1.52 < |\eta^{\gamma}| < 1.81$

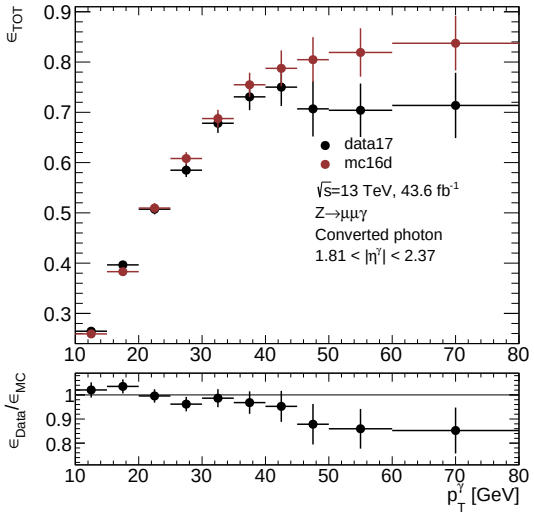

(d) $1.81 < |\eta^{\gamma}| < 2.37$

Figure 32: Comparison of data-driven and MC total efficiency measurements for events with muons and a converted photon as a function of p_T^{γ}, for the four pseudorapidity bins. The error bars show statistical uncertainty only.

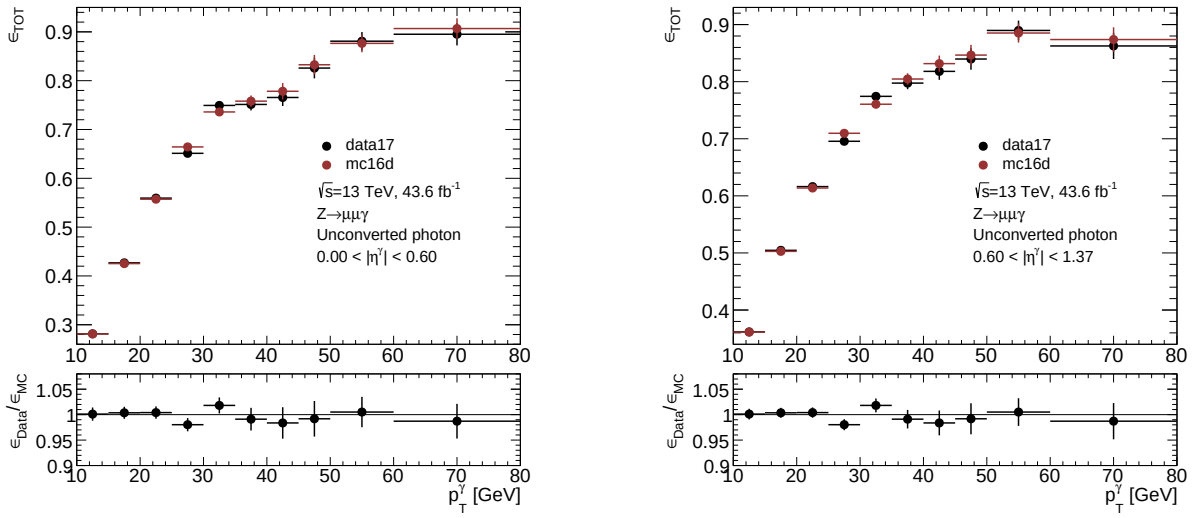

(a) $0.0 < |\eta^{\gamma}| < 0.6$

(b) $0.6 < |\eta^{\gamma}| < 1.37$

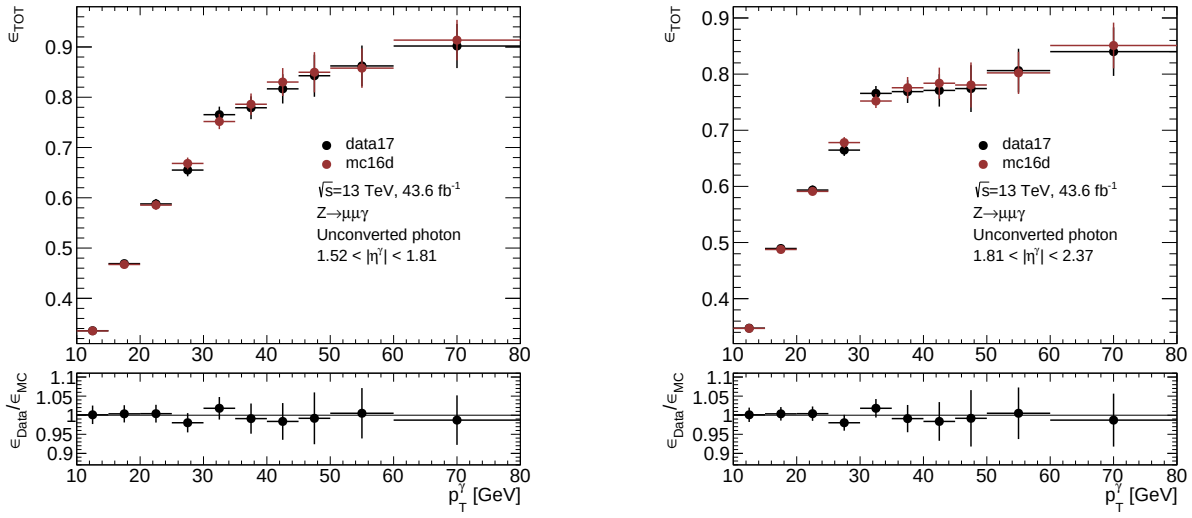

(c) $1.52 < |\eta^{\gamma}| < 1.81$

(d) $1.81 < |\eta^{\gamma}| < 2.37$

Figure 33: Comparison of data-driven and MC total efficiency measurements for events with muons and an unconverted photon as a function of p_T^{γ}, for the four pseudorapidity bins. The error bars show statistical uncertainty only.

9 Further work

9.1 Reducible background modelling

Figures 34 and 35 demonstrate the poor quality of the DSCB fit to the CR data for $p_T^{\gamma} < 20$ GeV. The DSCB does not approximate the data shape well at $m_{\ell\ell\gamma} < 90$ GeV. The fit is better for $p_T^{\gamma} > 20$ GeV, but could still be improved. This could be achieved by fitting the data to an alternative function. Functions that could be tested are Bernstein polynomials and a triple Gaussian.

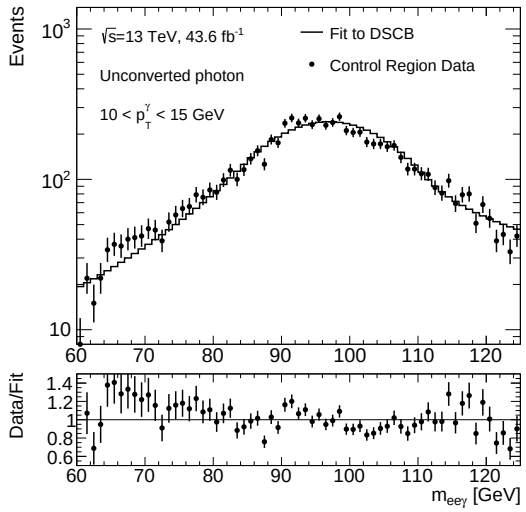

Figure 34: Fit of a DSCB to the $m_{\ell\ell\gamma}$ distribution of the CR data in the $10 < p_T^\gamma < 15$ GeV, electrons and unconverted photon bin. There is a significant difference between the data and the DSCB fit for $m_{\ell\ell\gamma} < 90$ GeV.

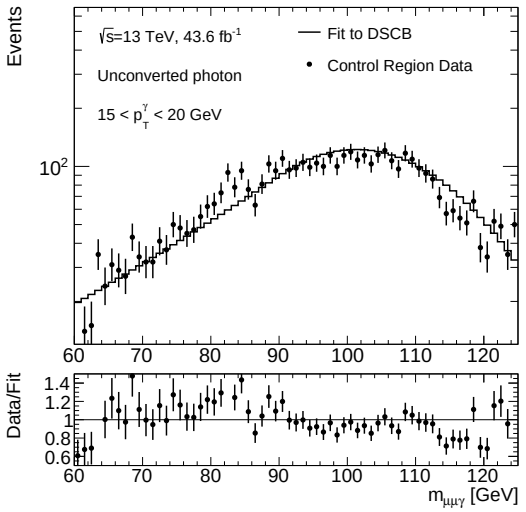

Figure 35: Fit of a DSCB to the $m_{\ell\ell\gamma}$ distribution of the CR data in the $10 < p_T^\gamma < 15$ GeV, electrons and unconverted photon bin. There is a significant difference between the data and the DSCB fit for $m_{\ell\ell\gamma} < 90$ GeV.

9.2 Missing background identification

Figure 36 demonstrates the large deficit in the Monte Carlo description of the data at $m_{\ell\ell\gamma} < 80$ GeV, $p_T^\gamma < 20$ GeV. This discrepancy is too large to be explained by the poor fitting of the DSCB (section 9.1). A likely cause is the lack of an irreducible background in the Monte Carlo description of the data, of which the most likely candidate is $\tau\tau\gamma$. This channel is expected to have 3% of the number of events as $Z \to \ell\ell\gamma$ (excluding the effects of event selection cuts) [8], which are expected to have $m_{\ell\ell\gamma}$ and p_T^γ values in the range where background is missing. Another possible missing irreducible background is $WW\gamma$, but this has a much smaller cross-section, so is not expected to be significant.

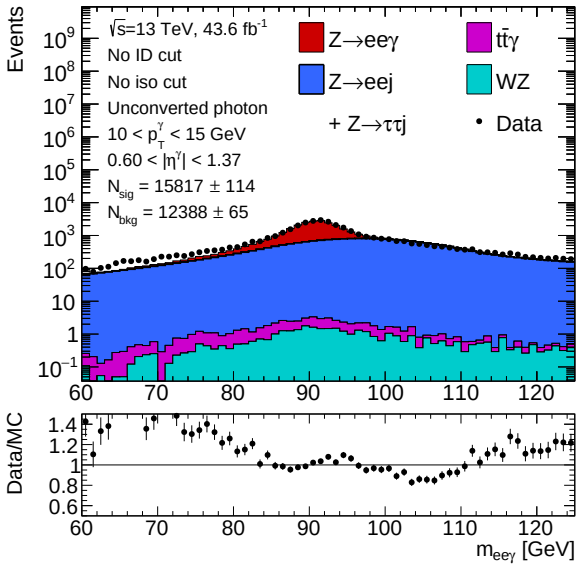

Figure 36: $m_{\ell\ell\gamma}$ distribution of events in the $10 < p_T^\gamma < 15$ GeV, $0.60 < |\eta^\gamma| < 1.37$, electrons and unconverted photon bin. The reducible background shape (dark blue) is from the DSCB fit. All templates are scaled as determined by the extended maximum likelihood fit. There is a large discrepancy between data and Monte Carlo at $m_{\ell\ell\gamma} < 80$ GeV.

9.3 Signal modelling

Statistical fluctuations in the signal template could be reduced by fitting the signal Monte Carlo to a PDF. The signal channel consists of two components: A large FSR component and the small tail of an ISR component. Therefore the PDF would have to be a sum of two functions; one to model the shape of each component.

Figure 37 depicts the evolution of the FSR and ISR components as minimum p_T^γ is increased: The FSR component moves to slightly lower $m_{\ell\ell}$ values and the ISR component moves to significantly higher $m_{\ell\ell\gamma}$ values. The progression of the FSR component suggests that the $40 < m_{\ell\ell} < 83$ GeV selection cut is only optimised for $p_T^\gamma < 20$ GeV and reducing the upper bound on this cut at $p_T^\gamma > 20$ GeV may improve exclusion of background here.

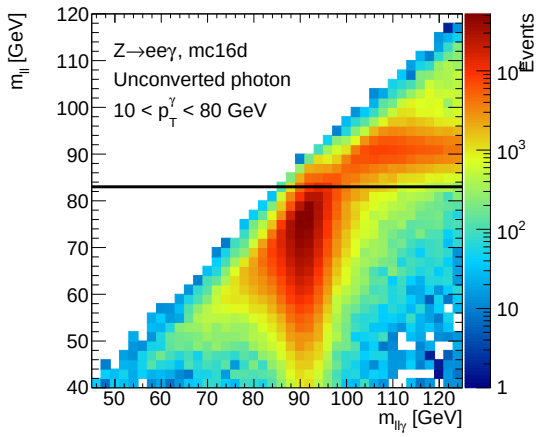

(a) $10 < p_T^\gamma < 80$ GeV. The vertical component at $m_{\ell\ell\gamma} \approx 90$ GeV is FSR and the horizontal component at $m_{\ell\ell} \approx 90$ GeV is ISR.

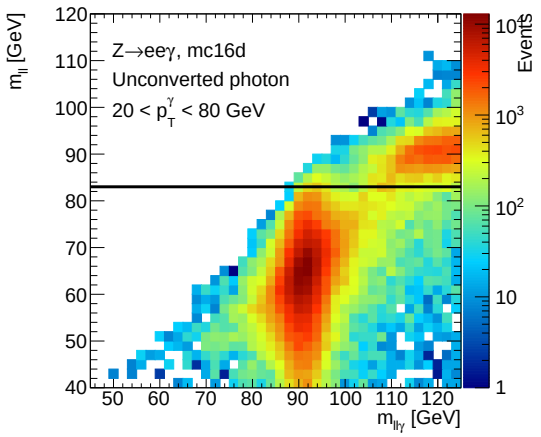

(b) $20 < p_T^\gamma < 80$ GeV. When the minimum p_T^γ is increased, the minimum $m_{\ell\ell\gamma}$ of ISR events also increases.

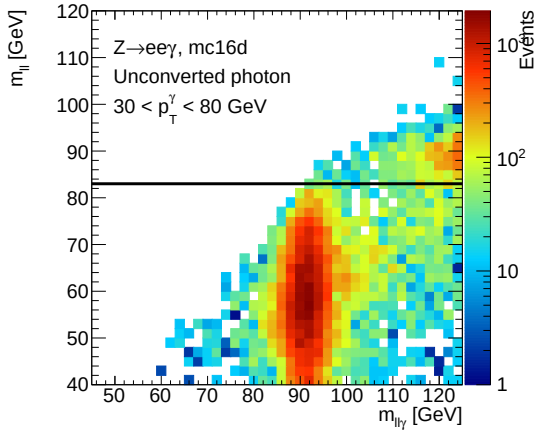

(c) $30 < p_T^\gamma < 80$ GeV.

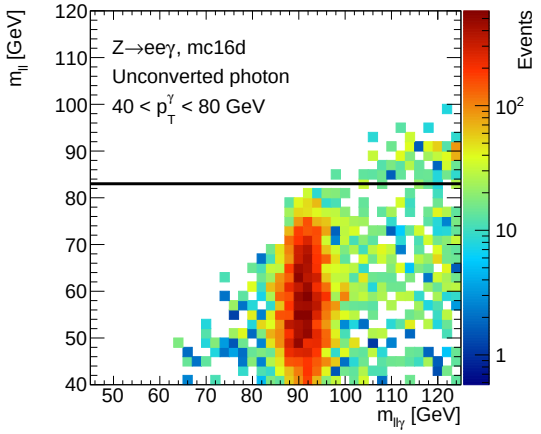

(d) $40 < p_T^\gamma < 80$ GeV. As a result of the minimum p_T^γ cut, almost no ISR events with $m_{\ell\ell\gamma} < 125$ GeV remain, and the FSR component has moved to lower $m_{\ell\ell}$ values.

Figure 37: Distribution of $Z \to ee\gamma$ events with an unconverted photon in $m_{\ell\ell}$-$m_{\ell\ell\gamma}$ space in different p_T^γ regions. Events above the line at $m_{\ell\ell} = 83$ GeV are excluded by selection cuts.

10 Conclusions

This report discusses potential improvements to the measurement of photon efficiencies using radiative Z decays, and presents the results of their implementation. Measurements of photon ID and total efficiencies approximately show the expected smooth, monotonic curve with higher efficiencies at higher p_T^γ. There is reasonable agreement between efficiencies derived from data and MC, but more comprehensive error estimates are required to make a full comparison.

The background channel $Z \to \tau\tau j$ is a significant contribution to the data set, and there is a fractional error of up to 0.4% on the ID efficiency and 2% on the total efficiency if it is not included. Therefore it is important to consider this channel in future measurements. The effects of the background channels WZ and $t\bar{t}\gamma$ are not significant compared to statistical and other systematic uncertainties, so do not need to be considered carefully in this measurement.

There is a deficit in the Monte Carlo description of the data in the region $p_T^\gamma < 20$ GeV,

$m_{\ell\ell\gamma} < 80$ GeV and this may be resolved by including the irreducible bacgkround $Z \to \tau\tau\gamma$. This channel is expected to be 3% of the size of $Z \to \ell\ell\gamma$ and have events primarily in this region. Therefore it is important to test this measurement with the inclusion of $Z \to \tau\tau\gamma$.

The statistical power of the reducible background template can be improved by using data from an anti-isolation, anti-ID control region rather than Monte Carlo and grouping all $|\eta^\gamma|$ bins. This is effective for $20 < p_T^\gamma < 40$ GeV, but the statistical power of the template is not good at higher p_T^γ, particularly for $m_{\ell\ell\gamma} < 80$ GeV. Statistical fluctuations can further be reduced by fitting the data to a smooth function. However, the fitting can be improved on what has been demonstrated here, particularly at $p_T^\gamma < 20$ GeV.

It is possible to calculate the total efficiency directly. However, this leads to large systematic uncertainties as a consequence of the high proportion of background in the denominator.

11 Acknowledgements

I am immensely grateful to my supervisor, Kurt Brendlinger, for all of the time, knowledge and encouragement offered throughout the course of this project. I would also like to thank Früd Braren, Daniel Rauch, Julian Schmöckel and Namgyun Jeong for their assistance and for many interesting discussions. The DESY ATLAS group have been incredibly welcoming, from the support offered to the many social gatherings. Thank you to the Summer Student Program organisers for providing the opportunity to work at DESY, where I have gained so much knowledge and become further inspired by Particle Physics. Finally, thank you to the other summer students for their wonderful friendship and support, and for joining me in some unforgettable experiences.

References

[1] ATLAS Collaboration. Measurement of the photon identification efficiencies with the ATLAS detector using LHC Run-2 data collected in 2015 and 2016. `https://cds.cern.ch/record/2290912`, Geneva, Oct 2017.

[2] Blocker, Craig. Uncertainties on Efficiencies. `https://www-cdf.fnal.gov/physics/statistics/notes/cdf7168_eff_uncertainties.ps`, Aug 2004.

[3] ATLAS Collaboration. Measurement of Higgs boson production in the diphoton decay channel in *pp* collisions at center-of-mass energies of 7 and 8 TeV with the ATLAS detector. *Physical Review D*, 90:112015, 2014.

[4] ATLAS Collaboration. Search for high-mass diphoton resonances in *pp* collisions at $\sqrt{s} =$ 8TeV with the ATLAS detector. *Physical Review D*, 92:032004, 2015.

[5] ATLAS Collaboration. Search for photonic signatures of gauge-mediated supersymmetry in 8 TeV *pp* collisions with the ATLAS detector. *Physical Review D*, 92:072001, 2015.

[6] ATLAS Collaboration. Measurement of the photon identification efficiencies with the ATLAS detector using LHC Run-1 data. *European Physical Journal C*, 76:666, 2016.

[7] ATLAS Collaboration. Measurement of the $W^\pm Z$ boson pair-production cross section in pp collisions at $\sqrt{s} = 13$ TeV with the ATLAS detector. *Physics Letters B*, 762:1–22, 2016.

[8] Particle Data Group. Review of Particle Physics. *Physical Review D*, 9:030001, 2018.

[9] Nadezda Proklova, Ilaria Luise, Giovanni Marchiori, Evgeny Soldatov, and Gregorio Bernardi. Photon identification efficiency measurements with radiative Z boson decays: Supporting documentation for the Photon identification in 2015 and 2016 ATLAS data. `https://cds.cern.ch/record/2255940`, Geneva, Mar 2017.

[10] W. Verkerke and D. Kirkby. The RooFit toolkit for data modeling. 2003.